# Universal features of the shape of elastic fibers in shear flow

Paweł J. Żuk<sup>1,2</sup>†, Agnieszka M. Słowicka<sup>1</sup>, Maria L. Ekiel-Jeżewska<sup>1</sup>‡ and Howard A. Stone<sup>2</sup>¶

<sup>1</sup>Institute of Fundamental Technological Research, Polish Academy of Sciences, ul. Pawinskiego 5b, 02-106 Warszawa, Poland

<sup>2</sup>Department of Mechanical and Aerospace Engineering, Princeton University, Princeton, New Jersey 08544, USA

(Received xx; revised xx; accepted xx)

We present a numerical study of the dynamics of an elastic fiber in a shear flow at low Reynolds number, and seek to understand several aspects of the fiber's motion using the equations for slender-body theory coupled to the elastica. The numerical simulations are performed in the bead-spring framework including hydrodynamic interactions in two theoretical schemes: the Generalized Rotne-Prager-Yamakawa model and a multipole expansion corrected for lubrication forces. In general, the two schemes yield similar results, including for the dominant scaling features of the shape that we identify. In particular, we focus on the evolution of an initially straight fiber oriented in the flow direction and show that the time scales of fiber bending, curling and rotation, which depend on its length and stiffness, determine the overall motion and evolution of the shapes. We document several characteristic time scales and curvatures representative of the shape that vary as power laws of the bending stiffness and fiber length. The numerical results are further supported by an interpretation using an elastica model.

**Key words:** low-Reynolds-number flows, Stokes equations, shear flow, flexible fibers, similarity, universal scaling

#### 1. Introduction

Physical systems that contain flexible fibers in flow are common in the processing needed to manufacture various textiles, which highlights the properties of fibrous suspensions, in biophysics and cell biology where flagella and cilia are responsible for motion and stirring of fluids and biopolymers constitute the matrix of the structural materials around cells, and in proposed microfabricated sensing technologies, among others. Three recent reviews describe the present state of the field (Lindner & Shelley 2015; du Roure et al. 2019; Witten & Diamant 2020). These kinds of problems pose challenges since the fluid motion is dictated, at least in part, by the shape of the filament, but the filament shape is itself determined by the flow. Here we study a viscous dominated, low-Reynolds-number flow where a flexible filament is confined to a plane. We document the response in a shear flow, where we focus on large deformations and quantify dominant features of the fiber shape as a function of its effective elasticity.

<sup>†</sup> Email address for correspondence: pjzuk@ippt.pan.pl

 $<sup>\</sup>ddagger$  Email address for correspondence: mekiel@ippt.pan.pl

<sup>¶</sup> Email address for correspondence: hastone@princeton.edu

Typically, fibers experience flow during both synthesis and application processes, and Poiseuille and shear flows are important and ubiquitous. Single fiber dynamics in shear and Poiseuille flows have been studied theoretically, numerically and experimentally and many different features have been elucidated in depth. In particular, there is a large literature on the hydrodynamics of individual rigid particles in shear flow starting with periodic motion of spheroids, analyzed by Jeffery (1922) and later extended for periodic and chaotic dynamics of more complex shapes by, for example, Bretherton (1962); Hinch & Leal (1979); Yarin et al. (1997); Wang et al. (2012); Thorp & Lister (2019).

The dynamics of rigid elongated particles changes significantly if an elastic deformation is included. In shear flows, the buckling process has been analyzed, e.g. by Forgacs & Mason (1959a); Hinch (1976); Becker & Shelley (2001), typical evolution of shapes has been investigated e.g. by Smith et al. (1999); Harasim et al. (2013); Nguyen & Fauci (2014); Słowicka et al. (2015); Liu et al. (2018); LaGrone et al. (2019), including knotted fibers (Matthews et al. 2010; Kuei et al. 2015; Narsimhan et al. 2017; Soh et al. 2018), and also deviations from Jeffery orbits have been studied, e.g. by Forgacs & Mason (1959b); Skjetne et al. (1997); LeDuc et al. (1999); Joung et al. (2001); Wang et al. (2012); Zhang et al. (2019); Zhang & Graham (2020); Słowicka et al. (2020).

In the Poiseuille flow, migration and accumulation of flexible fibers have been observed and studied, e.g. by Jendrejack et al. (2004); Ma & Graham (2005); Khare et al. (2006); Słowicka et al. (2012, 2013); Farutin et al. (2016). Also the influence of other types of flow (extensional, cellular, compressional) and bending stiffness on the shapes of deformed fibers have been studied (Kantsler & Goldstein 2012; Young & Shelley 2007; Wandersman et al. 2010; Chakrabarti et al. 2020). Related interesting research is on the rheology of non-spherical particles (Batchelor 1970b; Cichocki et al. 2012; Zuk et al. 2017), which is of importance in bio-sciences (de la Torre & Bloomfield 1978; Harding 1997; Zuk et al. 2018) and also includes new features caused by flexibility (Switzer III & Klingenberg 2003). In general, few have focused on typical time scales characteristic of the bending process of a single fiber in low-Reynolds-number flow, which is the focus of our work in the context of the shear flow.

Słowicka  $et\ al.\ (2020)$  demonstrated that in the shear flow, for a wide range of values of the bending stiffness ratio A, elastic fibers often tend to the flow-gradient plane if initially located out of it. More precisely, in (Słowicka  $et\ al.\ 2020$ ) fibers were initially straight, and hundreds of their 3D initial orientations spanned the whole range of 3D directions. It turned out that in most cases fibers perform effective time-dependent Jeffery orbits and are (exponentially in time) attracted to spinning along the vorticity direction or tumbling motion in the flow-gradient plane. The typical relaxation times are very long. In a certain range of A, there exists also an attracting 3D dynamical periodic mode. For larger values of A, the tumbling motion in the flow-gradient plane is the attractor for majority of the initial orientations. Therefore, in this paper we focus on the analysis of fibers that perform their motion entirely in the flow-gradient plane.

We use a numerical bead-spring model and theoretical elastica model to study a single elastic fiber in a low-Reynolds-number shear flow. In particular, we perform extensive bead-spring simulations with n=20-300 beads and two different models of the constitutive relations that determine the resistance of the fiber to bending, i.e., the bead-bead elastic potential energy, and two different models of hydrodynamic interactions. The parameters allow for high aspect ratio, highly flexible fibers. In addition to these bead-spring simulations, we use the elastica and slender-body descriptions of the flexible fiber deformation to rationalize the dynamics.

We characterize the dynamics evaluated numerically from the bead-spring model by identifying typical time scales of the shape deformation and the maximum curvatures that

represent the flexible fiber. As one example, we identify a bending time scale intrinsic to the end of a fiber that begins to slowly bend from a straight configuration aligned with the flow direction. The displacement is caused by a transverse force at the end induced by hydrodynamic interactions caused by the rate-of-strain of the flow. Then, due to this small displacement, in the shear flow a tensile force builds up in the tip region, and eventually a rapid buckling of the tip takes place.

The tumbling motion of a flexible fiber initially aligned with the flow have been analyzed in many previous publications, numerically and experimentally, e.g. by Forgacs & Mason (1959a); Yamamoto & Matsuoka (1993); Skjetne et al. (1997); Lindström & Uesaka (2007); Słowicka et al. (2012, 2013, 2015, 2020); Harasim et al. (2013); Nguyen & Fauci (2014); Farutin et al. (2016); Liu et al. (2018); LaGrone et al. (2019). This pattern of the dynamics, typical for elongated objects of a non-negligible thickness, is not reproduced by the inextensible infinitely thin Euler-Bernoulli beam (elastica), analyzed e.g. by Audoly (2015); Lindner & Shelley (2015). The elastica does not move out of the stationary configuration perfectly along the flow. Therefore, in this paper we introduce a modified model that accounts for the dynamics of elastica initially aligned with the shear flow and allows it to move out of the initial position. The key idea is to extend the Euler-Bernoulli beam model by adding a point force exerted on the end beads of the fiber in the direction perpendicular to the flow. This force is caused by the shear flow, in agreement with the standard theory of the hydrodynamic interactions Kim & Karrila (1991). Using the elastica model modified in this way, we construct an analytical solution of the early time dynamics, which is in excellent agreement with our numerical simulations.

Moreover, we identify several additional universal scaling laws of the fiber shape and dynamics from the numerical simulations and in some cases are able to rationalize the results using the elastica model. We observe that essential features of the fiber dynamics can be well understood using the parameter space of the fiber's bending stiffness and aspect ratio, which extends the concept of the elasto-viscous number.

This article is organized in the following way. We describe two bead-spring models,  $\mathcal{M}_1$  and  $\mathcal{M}_2$ , of a flexible fiber in §2.1. We specify elastic and hydrodynamic interactions in §2.1.1 and §2.1.2, respectively. We explain why the fiber made of beads aligned with the flow moves out of this position in §2.1.3. We evaluate the hydrodynamic force on the tip of the fiber aligned with the flow in §2.1.4. We present the elastica/slender-body theory in §2.2. A typical evolution of a flexible fiber, initially aligned with the shear flow, is shown in §3. Evolution of shape and its maximum curvature are used to introduce typical time scales. The limits of a small and a large ratio A of the bending stiffness to the corresponding viscous stresses associated with the shear flow are discussed. The evolution of the fiber at early times is analyzed in §4. Based on the numerical simulations, in §4.1 we demonstrate that the bending process originates from the fiber ends, and at early times only the fiber ends are deformed. We define the corresponding bending time  $\tau_b$  and show that it does not depend on the fiber aspect ratio n if n is large enough, and it scales as  $\tau_b \propto A^{1/3}$ . We also provide a scaling of  $\tau_b$  in the whole range of A and n. A similarity solution of small deformations and early times for the elastica is given in §4.2, and it is used for a comparison with the numerical bead-spring simulations in §4.3. The essential new input is the addition to the elastica model of a hydrodynamic force exerted on the fiber tip by the rate-of-strain of the shear flow, in a similar way as it follows from the bead-spring models of the hydrodynamic interactions. In §4.4 we demonstrate that the fiber shapes scale approximately with  $A^{1/3}$  for times  $t \leq \tau_b$ , even beyond the range of small deformations, and provide arguments from the elastica model.

Highly bent fibers, for  $t \ge \tau_b$ , are analyzed in §5. From the numerical simulations

based on the bead models  $\mathcal{M}_1$  and  $\mathcal{M}_2$  we demonstrate in §5.1 that the maximum fiber curvature  $\kappa_{b2}$  over time is a local quantity - it does not depend on n if the fiber is long enough, and it satisfies a power law dependence on A. An explanation for the results in terms of the elastica, and also other numerically found scaling laws, are given in §5.2. Curling motion of a highly bent fiber is analyzed with the  $\mathcal{M}_1$  bead model and scaling laws for the curling velocity along the flow are presented in §5.3.

Characteristic features of the fiber dynamics and curvature in the phase space of the aspect ratio n and the bending stiffness ratio A are analyzed in §6 with the use of the bead models  $\mathcal{M}_1$  and  $\mathcal{M}_2$ . The universal similarity scaling of the maximum curvature  $\kappa_{b2}$  is provided in §6.1. The phase space diagram of the dynamical modes is found in §6.2. The distinction between the fibers that bend locally (for larger n and smaller A), and the fibers that bend globally (for smaller n and larger n is demonstrated. The transition between them is shown to take place gradually in a certain range of the phase space. In contrast, within the local bending mode, there exists a sharp transition in the phase space between the fibers that straighten out along the flow while tumbling and the fibers that stay coiled. The transition is described by a simple scaling law. The final conclusions are outlined in §7. In addition, we give the details of the theoretical and numerical description of the hydrodynamic interactions between the fiber beads in Appendix A, compare the results obtained by the theoretical models  $\mathcal{M}_1$  and  $\mathcal{M}_2$  in Appendix B, discuss the universal similarity scaling and the transition between local and global bending in Appendices C and D, respectively.

#### 2. Model of the fiber

We consider the low-Reynolds-number motion of a neutrally buoyant elastic fiber in a fluid of viscosity  $\mu_0$ . In particular, the interaction of an elastic fiber with an external shear flow

$$\mathbf{V}_{\infty}(\mathbf{R}) = (\dot{\gamma}Z, 0, 0), \tag{2.1}$$

with  $\mathbf{R} = (X, Y, Z)$ , is a nonlinear problem and many approaches have been devised to study it theoretically and numerically, e.g. bead-spring models (Warner 1972; Larson et al. 1999; Kuei et al. 2015; Słowicka et al. 2015, 2020), cylinder-hinge models (Schmid & Klingenberg 2000; Férec et al. 2009), slender-body and inextensible Euler-Bernoulli beams (elastica) approaches (Tornberg & Shelley 2004; Nazockdast et al. 2017; Becker & Shelley 2001; Liu et al. 2018), the boundary integral technique (Peskin 2002), the method of regularized Stokeslets (Cortez et al. 2005; Nguyen & Fauci 2014; LaGrone et al. 2019), etc. We exploit the bead-spring approach for numerical simulations and the elastica model for rationalization of the numerical results (see figure 1).

#### 2.1. Bead model

The bead-spring model illustrated in figure 1(a) describes elastic and hydrodynamic interactions between n numbered i=1,...,n spherical beads of identical radii a (ith bead position is denoted as  $\mathbf{R}_i$ ). In this work, we use three different bead models  $\mathcal{M}_i$ , i=1,2,3 (cf. Table 1), which include combinations of two different descriptions of hydrodynamic interactions (HI), described below and in Appendix A: the Generalized Rotne-Prager-Yamakawa (GRPY) method (Wajnryb et al. 2013; Zuk et al. 2017) and the multipole method with lubrication correction (HYDROMULTIPOLE) (Cichocki et al. 1999; Ekiel-Jeżewska & Wajnryb 2009) with two sets of constitutive laws specifying elastic interactions that are described next.

The results presented in the following sections are based on the numerical simula-

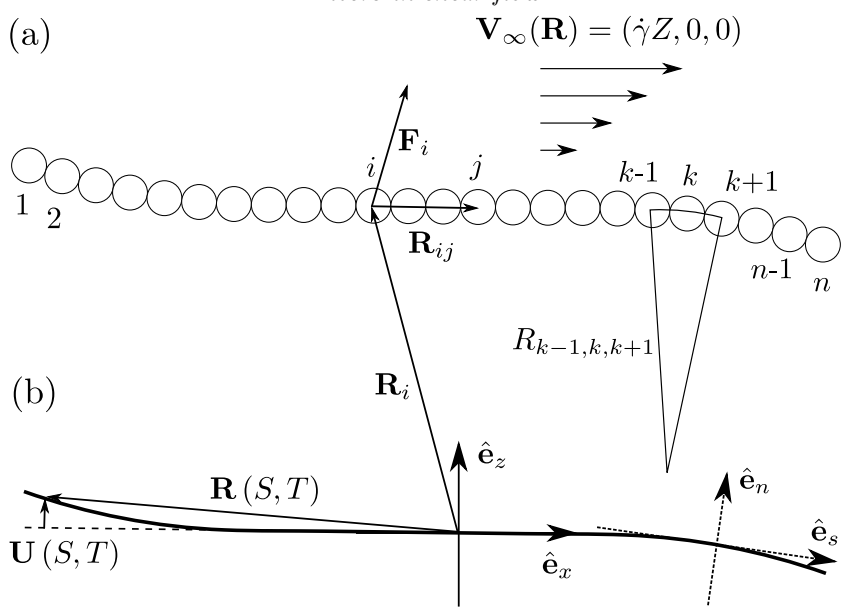


FIGURE 1. Models of a fiber in shear flow and the notation. (a) The bead model. (b) The elastica model.

HI model	constitutive laws	
	set 1	set 2
	Eqs. $(2.2),(2.3)$	Eqs. $(2.4),(2.5)$
GRPY + Eq. (2.6)	$\mathcal{M}_1$	$\mathcal{M}_3$
Hydromultipole		$\mathcal{M}_2$

Table 1. Physical assumptions of the bead-spring models  $\mathcal{M}_1$ ,  $\mathcal{M}_2$  and  $\mathcal{M}_3$ .

tions from the bead models  $\mathcal{M}_1$  and  $\mathcal{M}_2$ . Both of them have the same long-distance asymptotics of the hydrodynamic interactions, and for close beads the HYDROMULTIPOLE method is more precise than the GRPY. However, the computations based on the HYDROMULTIPOLE algorithm require more time and memory than the GRPY approach. The GRPY model has been therefore used in simulations of very long fibers. For  $n \leq 100$  both  $\mathcal{M}_1$  and  $\mathcal{M}_2$  have been applied.

Qualitative results from the bead-spring models  $\mathcal{M}_1$  and  $\mathcal{M}_2$  are similar and in regimes of large A and n they are also the same quantitatively. A detailed comparison of the results obtained within both models is given in Appendix B. The model  $\mathcal{M}_3$  (see table 1) is applied there to explain that some differences between the models  $\mathcal{M}_1$  and  $\mathcal{M}_2$  are related to different expressions for the bending potential energy, in agreement with the predictions of Bukowicki & Ekiel-Jeżewska (2018).

#### 2.1.1. Elastic interactions

An elastic interaction potential model (constitutive laws) specifies a sum  $\mathcal{E}$  of all beadbead interaction energies, which are used to calculate elastic forces  $\mathbf{F}_i = -\nabla_{\mathbf{R}_i} \mathcal{E}$  acting on each bead i. We assume that there are no elastic torques acting on the beads. For

every pair of beads i, j the connector vector  $\mathbf{R}_{ij} = \mathbf{R}_j - \mathbf{R}_i$  points from the center of the sphere i towards the center of sphere j.

For the first set of constitutive laws, set 1, between the centers of every two consecutive beads i and i + 1 we impose the FENE (finitely extensible nonlinear elastic) stretching potential energy (Warner 1972)

$$E_{s,ij} = \frac{k_s' R_m^2}{2} \log \left[ 1 - \left( \frac{R_{ij} - 2a}{R_m} \right)^2 \right],$$
 (2.2)

where j = i + 1,  $k'_s$  is the spring stiffness,  $R_m = 0.2a$  is the maximum stretching from the equilibrium distance and  $R_{ij} = |\mathbf{R}_{ij}|$ . Between every triplet of beads i - 1, i, i + 1 we impose a harmonic bending potential energy,

$$E_{b,i} = \frac{A'}{2} (\theta_0 - \theta_i)^2, \tag{2.3}$$

where  $\theta_i$  and  $\theta_0$  are, respectively, the time-dependent and the equilibrium angles between connector vectors  $\mathbf{R}_{i,i-1}$  and  $\mathbf{R}_{i,i+1}$ , and  $A' = EI/L_0$  is the bending stiffness (per unit length), with the Young modulus E, the moment of inertia  $I = \pi a^4/4$ , and the distance  $L_0$  between the centers of the consecutive beads. Because a fiber is straight, when in equilibrium, the angle  $\theta_0 = \pi$ . In the set 1 of the constitutive laws we assume that  $L_0 = 2a$ .

For the second set of constitutive laws, set 2, between centers of every two consecutive beads i and i + 1 we impose a harmonic stretching potential energy

$$E_{s,ij} = \frac{k_s'}{2} (R_{ij} - L_0)^2, \tag{2.4}$$

with j = i + 1 and the equilibrium distance  $L_0$  between the bead centers usually close to  $R_0 = 2a$  but a bit larger. Between every triplet of beads i - 1, i, i + 1 we impose a cosine (Kratky-Porod) bending potential energy

$$E_{b,i} = A' \left( 1 + \frac{\mathbf{R}_{i,i-1} \cdot \mathbf{R}_{i,i+i}}{|\mathbf{R}_{i,i-1}||\mathbf{R}_{i,i+i}|} \right) = A' (1 + \cos \theta_i).$$
 (2.5)

This potential energy is a widely used discrete approximation of the elastic bending stiffness, see e.g. Gauger & Stark (2006).

Additionally when the GRPY model of hydrodynamic interactions is used we add the repulsive part of the Lennard-Jones potential energy

$$E_{R,ij} = 4\epsilon'_{LJ} \left(\frac{\sigma_{LJ}}{R_{ij}}\right)^{12} \tag{2.6}$$

between the second nearest or further neighbor beads, where  $\epsilon'_{LJ}$  determines the strength of the potential and  $\sigma_{LJ}$  is the characteristic distance. We set  $\sigma_{LJ} = 2a$  and truncate the Lennard-Jones interaction range to  $2.5\sigma_{LJ}$ . This potential acts to prevent large overlaps of the beads (comparable with  $2a - R_{ij} \ll a$  for  $R_{ij} < 2a$ ). This is not necessary for the Hydromultipole model because the lubrication forces prevent the beads from overlapping.

#### 2.1.2. Hydrodynamic interactions

In this work, we study translational motion of segments of a flexible fiber. In the framework of the bead-spring modeling the translational motion of the fiber beads is determined by the theory of hydrodynamic interactions between spherical particles. We consider n spherical particles in a fluid of viscosity  $\mu_0$  subject to an incompressible

external flow  $V_{\infty}(\mathbf{r})$ . We investigate the case where the Reynolds number is much smaller than unity and the quasi-steady fluid velocity  $V(\mathbf{R})$  and pressure  $p(\mathbf{R})$  are described by the Stokes equations (Kim & Karrila 1991; Oseen 1927).

The theory of hydrodynamic interactions is used to calculate the translational velocities  $U_i$  of the particles, which are in turn necessary to integrate the particle trajectories. In our case the external flows are linear, and there are no torques applied to the particles. Therefore the translational velocities  $U_i$  satisfy the relations,

$$U_i = \mathbf{V}_{\infty}(\mathbf{R}_i) + \sum_{j=1}^{n} \left( \boldsymbol{\mu}_{ij}^{tt} \cdot \mathbf{F}_j + \boldsymbol{\mu}_{ij}^{td} : \mathbf{E}_{\infty} \right), \tag{2.7}$$

where  $\mathbf{F}_j$  is the total external force exerted on the particle j and  $\mathbf{E}_{\infty} = (\nabla \mathbf{V}_{\infty} + (\nabla \mathbf{V}_{\infty})^T)/2$  denotes the rate-of-strain tensor of the external fluid flow  $\mathbf{V}_{\infty}$ . For the shear flow given by equation (2.1),

$$\mathbf{E}_{\infty} = \frac{\dot{\gamma}}{2} \begin{pmatrix} 0 & 0 & 1\\ 0 & 0 & 0\\ 1 & 0 & 0 \end{pmatrix}. \tag{2.8}$$

There are different methods to evaluate the translational-translational  $\mu_{ij}^{tt}$  and translational-dipolar  $\mu_{ij}^{td}$  mobility matrices. The most precise is the multipole expansion, corrected for lubrication, in order to speed up the convergence (Durlofsky *et al.* 1987; Sangani & Mo 1994; Cichocki *et al.* 1994, 1999; Ekiel-Jeżewska & Wajnryb 2009) through the inverse-power expansion in the inter-particle distance (Kim & Karrila 1991). The analytical Rotne-Prager-Yamakawa approximation is also often used (Rotne & Prager 1969).

In this work we evaluate the mobility matrices as functions of positions of all the beads using two methods outlined in Appendix A. First, we apply the analytical Rotne-Prager-Yamakawa approximation of the translational-translational mobility  $\mu_{ij}^{tt}$  (Rotne & Prager 1969), generalized also for the translational-dipole mobility matrix  $\mu_{ij}^{td}$  (Kim & Karrila 1991) and implemented in the GRPY numerical program. Second, we use the precise multipole method corrected for lubrication, implemented in the numerical code Hydromultipole. The GRPY procedure is less precise, when particle surfaces are closer than the radius of the smaller particle, but computationally much faster then the Hydromultipole algorithm. Both methods will be briefly outlined in Appendix A.

The equations of motion for the positions  $\mathbf{R}_i$  of the beads are

$$\dot{\mathbf{R}}_i = \mathbf{U}_i,\tag{2.9}$$

with  $U_i$  dependent on the positions  $\mathbf{R}_j$  of all the bead centers j = 1, ..., n, and given by equation (2.7).

The equations of motion (2.9) are solved numerically with the use of dimensionless variables. We choose as a characteristic length the bead diameter 2a. The total length of the fiber at equilibrium is L, which in the case of the  $\mathcal{M}_1$  model is fixed to L=2na so that the fiber aspect ratio is n. We choose as a time scale the inverse of the shear rate  $\dot{\gamma}^{-1}$  and the forces are normalized with  $\pi \mu_0 \dot{\gamma}(2a)^2$ . The above introduces the dimensionless stretching stiffness  $k_s = k_s'/(\pi \mu_0 \dot{\gamma}(2a))$ ,  $\epsilon_{LJ} = \epsilon_{LJ}'/(\pi \mu_0 \dot{\gamma}(2a)^3)$  and the bending stiffness

$$A = A'/(\pi \mu_0 \dot{\gamma}(2a)^3) = EI/(\pi \mu_0 \dot{\gamma} L_0(2a)^3). \tag{2.10}$$

For the GRPY approach,  $L_0 = 2a$ . Note that for the HYDROMULTIPOLE treatment of the hydrodynamic interactions, the dimensionless bending stiffness ratio A used here is slightly different from the corresponding parameter  $EI/(\pi\mu_0\dot{\gamma}(2a)^4)$  used by Słowicka

et al. (2013, 2015, 2020) and denoted there by the same letter. To adjust for this difference, all the numerical values of the bending stiffness based on the HYDROMULTIPOLE codes taken from earlier works were in this paper divided by  $L_0/(2a)$  (typically equal to 1.02 or 1.01, see Appendix B).

#### 2.1.3. Why a fiber aligned with the flow moves out of this position

To answer this question, we will use equation (2.7) to analyze velocities of the beads for a fiber aligned with the flow and at the elastic equilibrium. We will use the standard pairwise-additive Rotne-Prager-Yamakawa (RPY) approximation for the distinct mobility matrices  $\mu_{ij}^{tt}$  and  $\mu_{ij}^{td}$  with  $i \neq j$  (Kim & Karrila 1991). From the geometric symmetry we can write down the tensorial form of the mobility matrices for a pair of particles i and j (Kim & Karrila 1991),

$$\boldsymbol{\mu}_{ij}^{tt} = A(R_{ij})\mathbf{d}_{ij}\mathbf{d}_{ij} + B(R_{ij})(\mathbf{I} - \mathbf{d}_{ij}\mathbf{d}_{ij}), \tag{2.11a}$$

$$\boldsymbol{\mu}_{ij}^{td} = C(R_{ij}) \left( \mathbf{d}_{ij} \mathbf{d}_{ij} - \frac{1}{3} \mathbf{I} \right) \mathbf{d}_{ij} + D(R_{ij}) \overline{\mathbf{d}_{ij} (\mathbf{I} - \mathbf{d}_{ij} \mathbf{d}_{ij})}, \tag{2.11b}$$

where **I** is the unit tensor,  $\mathbf{d}_{ij} = \mathbf{R}_{ij}/|\mathbf{R}_{ij}|$ , and  $\overline{\mathbf{d}_{ij}(\mathbf{I} - \mathbf{d}_{ij}\mathbf{d}_{ij})}$  is a third rank tensor symmetric and traceless in the first and second Cartesian components, i.e.,  $\overline{\mathbf{d}_{ij}(\mathbf{I} - \mathbf{d}_{ij}\mathbf{d}_{ij})}_{\alpha\beta\gamma} = \frac{1}{2} \left(d_{\alpha}\delta_{\beta\gamma} + d_{\beta}\delta_{\alpha\gamma}\right) - d_{\alpha}d_{\beta}d_{\gamma}$ , where the Cartesian components are labeled with the Greek letters. Within the RPY approximation, the translational-translational self-mobility matrix

$$\boldsymbol{\mu}_{ii}^{tt} = \frac{1}{6\pi\mu_0 a} \mathbf{I} \tag{2.12}$$

and the translational-dipolar self-mobility matrix vanishes,  $\mu_{ii}^{td} = 0$ .

Our goal now is to investigate the initial configuration, when the fiber is parallel to the flow. In this case  $\mathbf{d}_{ij} = \pm \hat{\mathbf{e}}_x$ , with the minus sign for the beads with labels i > j. Since the fiber is at the elastic equilibrium, the external forces vanish,  $\mathbf{F}_j = \mathbf{0}$ , and the only contribution to velocity in the direction perpendicular to the flow comes from the translational-dipolar mobility. From equation (2.11b) it follows that the contribution to the velocity  $U_i$  of particle i from the translational-dipolar mobility  $\mu_{ij}^{td}$  acting on the strain tensor  $\mathbf{E}_{\infty}$  (where  $[\mathbf{A}:\mathbf{B}]_{ij} = A_{ik}B_{kj}$ ) consists of two terms proportional to

$$(\mathbf{d}_{ij}\mathbf{d}_{ij} - \frac{1}{3}\mathbf{I})\mathbf{d}_{ij} : \mathbf{E}_{\infty} = \frac{\dot{\gamma}}{2} \begin{pmatrix} 0 \\ 0 \\ 1/3 \end{pmatrix} \text{ and } \overline{\mathbf{d}_{ij}(\mathbf{I} - \mathbf{d}_{ij}\mathbf{d}_{ij})} : \mathbf{E}_{\infty} = \frac{\dot{\gamma}}{2} \begin{pmatrix} 0 \\ 0 \\ -1 \end{pmatrix}, (2.13)$$

respectively. Therefore, there exist contributions to the bead velocities perpendicular to the flow, and this is why the fiber moves out of the position aligned with the flow. In the next section, we will show that the largest are perpendicular velocities of the first and last beads, at the initial configuration aligned with the flow, and also later when the fiber is slightly deflected. We will also demonstrate that this effect can be considered as the result of a hydrodynamic force exerted by the shear flow on the fiber.

#### 2.1.4. Hydrodynamic force acting on the tip of the fiber initially aligned with the flow

We now move on to the discussion of the hydrodynamic force exerted by the shear flow on the tip of a fiber aligned with the flow or already slightly deflected from the alignment. In the following, we are going to provide the theoretical explanation for the initial stage of the bending process in terms of the elastica, based on the assumption that a constant hydrodynamic force is exerted on the fiber end by the shear flow. In the standard use of the elastica equations the existence of such a force has not been yet taken into account. Here we use the general framework of the theory of hydrodynamic interactions presented in the previous sections to explain the physical origin of this force, and to estimate its value numerically (with the bead model  $\mathcal{M}_1$ ).

In the bead models, the tip force can be found rewriting equation (2.7)

$$\dot{\mathbf{R}}_{i} - \mathbf{V}_{\infty}(\mathbf{R}_{i}) = \boldsymbol{\mu}_{ii}^{tt} \cdot \left( \mathbf{F}_{i} + (\boldsymbol{\mu}_{ii}^{tt})^{-1} \sum_{j} \boldsymbol{\mu}_{ij}^{td} : \mathbf{E}_{\infty} \right) + \sum_{j \neq i} \left( \boldsymbol{\mu}_{ij}^{tt} \cdot \mathbf{F}_{j} \right), \tag{2.14}$$

where  $\mu_{ii}^{tt}$  is the translational self-mobility matrix, and defining the hydrodynamic force acting on bead i as

$$\mathbf{F}_{Hi} = (\boldsymbol{\mu}_{ii}^{tt})^{-1} \sum_{j} \boldsymbol{\mu}_{ij}^{td} : \mathbf{E}_{\infty}. \tag{2.15}$$

The dimensionless form is  $\mathbf{f}_{Hi} = \mathbf{F}_{Hi} / (\pi \mu_0 \dot{\gamma}(2a)^2)$ .

Our goal is to investigate  $\mathbf{F}_{Hi}$  at the early stage of the evolution, when the fiber, initially aligned with the flow, slowly moves out of this configuration, but still remains almost parallel to the flow. We will now show that for the fiber almost aligned with the flow, the hydrodynamic forces  $\mathbf{F}_{Hi}$ , defined by equation (2.15), are almost perpendicular to the flow direction  $\hat{\mathbf{e}}_x$ . We will also provide some theoretical arguments why the value of  $\mathbf{F}_{Hi}$  is the largest at the ends of the fiber.

The hydrodynamic forces  $\mathbf{F}_{Hi}$  given by (2.15) are proportional to the shear rate  $\dot{\gamma}$ . Moreover, the force  $\mathbf{F}_{Hi}$  is perpendicular to the flow and parallel to the z direction of the flow gradient,  $\mathbf{F}_{Hi} \approx \hat{\mathbf{e}}_z \cdot \mathbf{F}_{Hi} \, \hat{\mathbf{e}}_z$ . Therefore they displace the fiber beads away from the position aligned with the flow. From the explicit expressions for the functions C and D in equation (2.11b), given e.g. by (Kim & Karrila 1991), it follows that for the first bead  $\hat{\mathbf{e}}_z \cdot \mathbf{F}_{H1} > 0$  and for the last bead  $\hat{\mathbf{e}}_z \cdot \mathbf{F}_{Hn} < 0$ . This means that, owing to the hydrodynamic forces (2.15), the fiber follows the rotational component of the shear flow.

hydrodynamic forces (2.15), the fiber follows the rotational component of the shear flow. It is also known that  $C \propto R_{ij}^{-2}$  and  $D \propto R_{ij}^{-4}$ , see e.g. Kim & Karrila (1991). Therefore, the major contribution to  $F_{Hi}$  comes from relatively close beads j. Additionally,  $\mu_{ij}^{td}$  is antisymmetric in  $\mathbf{d}_{ij}$ , which means that the terms in (2.15) corresponding to equally distant left and right neighbors will cancel. Therefore, the total force  $F_{Hi}$  is close to zero for i in the middle part of the fiber, and it increases when i is closer to the fiber ends. For longer fibers, the force  $F_{Hi}$  is non-negligible only for i close to one of the fiber ends, and it only weakly depends on the total fiber length because it comes from unbalanced local interactions between the bead i and close beads j.

To evaluate  $\mathbf{f}_{Hi}$  numerically, we use the pairwise-additive GRPY approximation for the mobility matrices. As argued above, in the stage when fiber is only slightly deflected from the straight line, at leading order,  $\mathbf{f}_{Hi}$  is directed along  $\hat{\mathbf{e}}_z$ . In figure 2(a) we plot the dimensionless hydrodynamic force  $\hat{\mathbf{e}}_z \cdot \mathbf{f}_{Hi}$  as a function of the bead label i for three different fiber lengths n. It is clear that the force is well-localized close to the fiber ends.

The orientation of  $\mathbf{f}_{Hi}$  follows the rotational component of the shear flow. As the fiber gets longer, the force is more localized. Regardless of the fiber length, the end beads support the largest forces, an order of magnitude larger then the forces acting on the other beads. The magnitude of the force acting on the first bead,  $\mathbf{f}_{H1} \cdot \hat{\mathbf{e}}_z$ , initially changes non-monotonically as a function of n (see figure 2(b)), until it reaches a limiting value  $f_H \approx 0.16$ . Indeed, we observe a localized, length independent tip force perpendicular to the flow. We will use this observation later to construct a modified elastica model, applicable for a fiber initially aligned with the flow. Now it is time to present the standard Euler-Bernoulli beam, based on the local slender-body theory.

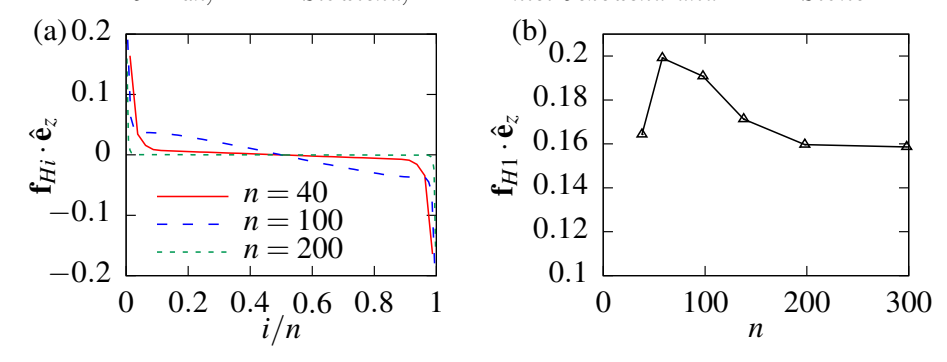


FIGURE 2. Hydrodynamic forces normal to the fiber, acting on beads i, calculated from Eq. (2.15) with the GRPY model of the hydrodynamic interactions. (a) Spatial distribution of the forces on the beads along the fiber. (b) The force on the first bead as a function of the fiber length n.

#### 2.2. The elastica and local slender-body theory

To rationalize the results of numerical simulations from the bead-spring simulations the inextensible elastica model (Duprat & Stone 2015; Lindner & Shelley 2015) is used with the local slender-body theory (SBT) (Cox 1970; Keller & Rubinow 1976; Johnson 1980) to account for the drag forces acting along the fiber. Within the local SBT, in contrast to the bead models, the full long-ranged hydrodynamic interactions are not incorporated, nor is the finite but small thickness of the filament. The last feature is especially important for fibers that are aligned with the flow, as it will be discussed in detail later. Similarly as in the bead model, for the elastica we also neglect Brownian motion and buoyancy forces. The fiber has a circular cross section of radius a and length L=2na where  $\epsilon=\frac{a}{L}=\frac{1}{2n}\ll 1$ . We denote as  $\mathbf{R}(S,T)$  the dimensional position of a fiber segment at the arc length S at time T. The equation of motion of each filament segment as a result of the applied elastic force density  $\mathbf{F}(S,T)$  per unit length, under the steady undisturbed flow  $\mathbf{V}_{\infty}$  can be expressed using the slender-body theory (Cox 1970; Duprat & Stone 2015; Lindner & Shelley 2015)

$$\dot{\mathbf{R}} - \mathbf{V}_{\infty}(\mathbf{R}) = \frac{\ln(\epsilon^{-1})}{4\pi\mu_0} \left( \mathbf{I} + \mathbf{R}_S \mathbf{R}_S \right) \cdot \mathbf{F}(S, T)$$
 (2.16)

or alternatively

$$\frac{2\pi\mu_0}{\ln(\epsilon^{-1})} \left( 2\mathbf{I} - \mathbf{R}_S \mathbf{R}_S \right) \cdot \left( \dot{\mathbf{R}} - \mathbf{V}_{\infty}(\mathbf{R}) \right) = \mathbf{F}(S, T)$$
 (2.17)

where  $\dot{\mathbf{R}} = \frac{\partial \mathbf{R}}{\partial T}$ ,  $\mathbf{R}_S = \frac{\partial \mathbf{R}}{\partial S}$  and the relative motion of the filament is obtained by applying the mobility tensor, proportional to the anisotropic tensor  $(\mathbf{I} + \mathbf{R}_S \mathbf{R}_S)$ , to the elastic force  $\mathbf{F}(S,T)$  on the fiber. Here we consider shear flow  $\mathbf{V}_{\infty}(\mathbf{R}) = \dot{\gamma} \mathbf{Z} \hat{\mathbf{e}}_x$ , where  $\mathbf{Z} = \hat{\mathbf{e}}_z \cdot \mathbf{R}$ . For the elastic fiber we use the notation illustrated in figure 1(b), i.e.,  $\hat{\mathbf{e}}_n$  denotes a unit vector normal to the fiber in the shear plane and  $\hat{\mathbf{e}}_s$  denotes a unit vector tangent to the fiber. The inextensibility condition  $|\mathbf{R}_S| = 1$  results in  $\hat{\mathbf{e}}_s = \mathbf{R}_S$  and implies the Frenet formulas  $\frac{\partial \hat{\mathbf{e}}_s}{\partial S} = K \hat{\mathbf{e}}_n$ ,  $\frac{\partial \hat{\mathbf{e}}_n}{\partial S} = -K \hat{\mathbf{e}}_s$ , where K is the local curvature and we have assumed that the fiber shape is planar.

In the elastica model the elastic forces acting on the unit segment of the fiber are (Audoly & Pomeau 2000; Audoly 2015),

$$\mathbf{F}(S,T) = (-EIK_S\hat{\mathbf{e}}_n + \Sigma\hat{\mathbf{e}}_s)_S,\tag{2.18}$$

where  $\Sigma(S,T)$  is the tension in the filament (satisfying inextensibility), E is the Young modulus and I is the moment of inertia ( $I = \pi a^4/4$ ), as earlier. Alternatively, the force density per unit length can be expressed as  $\mathbf{F}(S,T) = -EI\mathbf{R}_{SSSS} + (\mathcal{T}\hat{\mathbf{e}}_s)_S$ , see e.g., Tornberg & Shelley (2004) and Lindner & Shelley (2015). It is easy to check that  $\Sigma = \mathcal{T} + EIK^2$ .

With the use of the Frenet formulas it is convenient to write separately the equations of motion in the normal and tangential directions, respectively,

$$\frac{4\pi\mu_0}{\ln(\epsilon^{-1})}\hat{\mathbf{e}}_n \cdot \left(\dot{\mathbf{R}} - \dot{\gamma}\hat{\mathbf{e}}_x(\hat{\mathbf{e}}_z \cdot \mathbf{R})\right) = -EIK_{SS} + \Sigma K, \tag{2.19a}$$

$$\frac{2\pi\mu_0}{\ln(\epsilon^{-1})}\hat{\mathbf{e}}_s \cdot \left(\dot{\mathbf{R}} - \dot{\gamma}\hat{\mathbf{e}}_x(\hat{\mathbf{e}}_z \cdot \mathbf{R})\right) = \left(\Sigma + \frac{EI}{2}K^2\right)_S. \tag{2.19b}$$

We write the dimensionless form (lowercase symbols) of equations (2.19) by expressing length in the units of 2a and time in the units  $\dot{\gamma}^{-1}$ , as in section 2.1, to find

$$\eta \hat{\mathbf{e}}_n \cdot (\dot{\mathbf{r}} - \hat{\mathbf{e}}_x(\hat{\mathbf{e}}_z \cdot \mathbf{r})) = -\kappa_{ss} + \sigma \kappa,$$
(2.20a)

$$\frac{\eta}{2}\hat{\mathbf{e}}_s \cdot (\dot{\mathbf{r}} - \hat{\mathbf{e}}_x(\hat{\mathbf{e}}_z \cdot \mathbf{r})) = \left(\sigma + \frac{1}{2}\kappa^2\right)_s, \tag{2.20b}$$

where

$$\eta = \frac{4\pi\mu_0(2a)^4\dot{\gamma}}{EI\ln(\epsilon^{-1})}\tag{2.21}$$

is a dimensionless compliance. Using the same normalization of EI as for the bead model,  $EI/(\pi\mu_0\dot{\gamma}L_0(2a)^3)$ , we can formally write  $\eta = \frac{4(2a)}{AL_0\ln(\epsilon^{-1})}$ . A physical comparison between the elastica and bead models will be presented in section 4.3.

The dimensionless compliance  $\eta$  is very similar to the elasto-viscous number  $\bar{\eta} = \frac{8\pi\mu_0L^4\dot{\gamma}}{EI\ln(\epsilon^{-1})}$  (Becker & Shelley 2001; Tornberg & Shelley 2004; Wandersman *et al.* 2010; Nguyen & Fauci 2014; Liu *et al.* 2018; du Roure *et al.* 2019; LaGrone *et al.* 2019). The main difference is that  $\bar{\eta}$  has the fiber's length L as the typical length scale, while  $\eta$  uses the fiber's radius.

# 3. A typical bead model simulation

The dimensionless stretching stiffness is fixed to a large value ( $k_s = 2000$  in the  $\mathcal{M}_1$  model and  $k_s = 1000$  in the  $\mathcal{M}_2$  model) so that the fiber is close to inextensible. In  $\mathcal{M}_1$ , the equilibrium distance between the bead centers corresponds to the touching beads,  $L_0 = 2a$  and the dimensionless Lennard-Jones potential coefficient  $\epsilon_{LJ} = 5$  allows only slight overlaps. In  $\mathcal{M}_2$ , lubrication interactions between close particle surfaces prevent overlaps. The equilibrium distance  $L_0$  between the bead centers has to be a bit larger than the bead diameter 2a; here we choose  $L_0/(2a) = 1.02$ . Sensitivity of the  $\mathcal{M}_2$  model to the choice of  $L_0$  has been discussed by Słowicka et al. (2015, 2020).

We focus on the fiber dynamics under the influence of the dimensionless bending stiffness A and the number of beads n, indicating the fiber's aspect ratio. The typical shape of a fiber during the evolution is presented in figure 3(a). The simulations (based on the  $\mathcal{M}_1$  model) start from a stretched fiber aligned in the flow direction. First we observe a slow deflection of the fiber tips up to time around 30. Later, until the time 35, rapid bending of the tip occurs. Next, a curling motion appears, with the maximum curvature moving to the central part of the fiber, and a typical shape is shown for t = 47. After the kinked parts of the fiber pass over each other (around time 62), the fiber rapidly

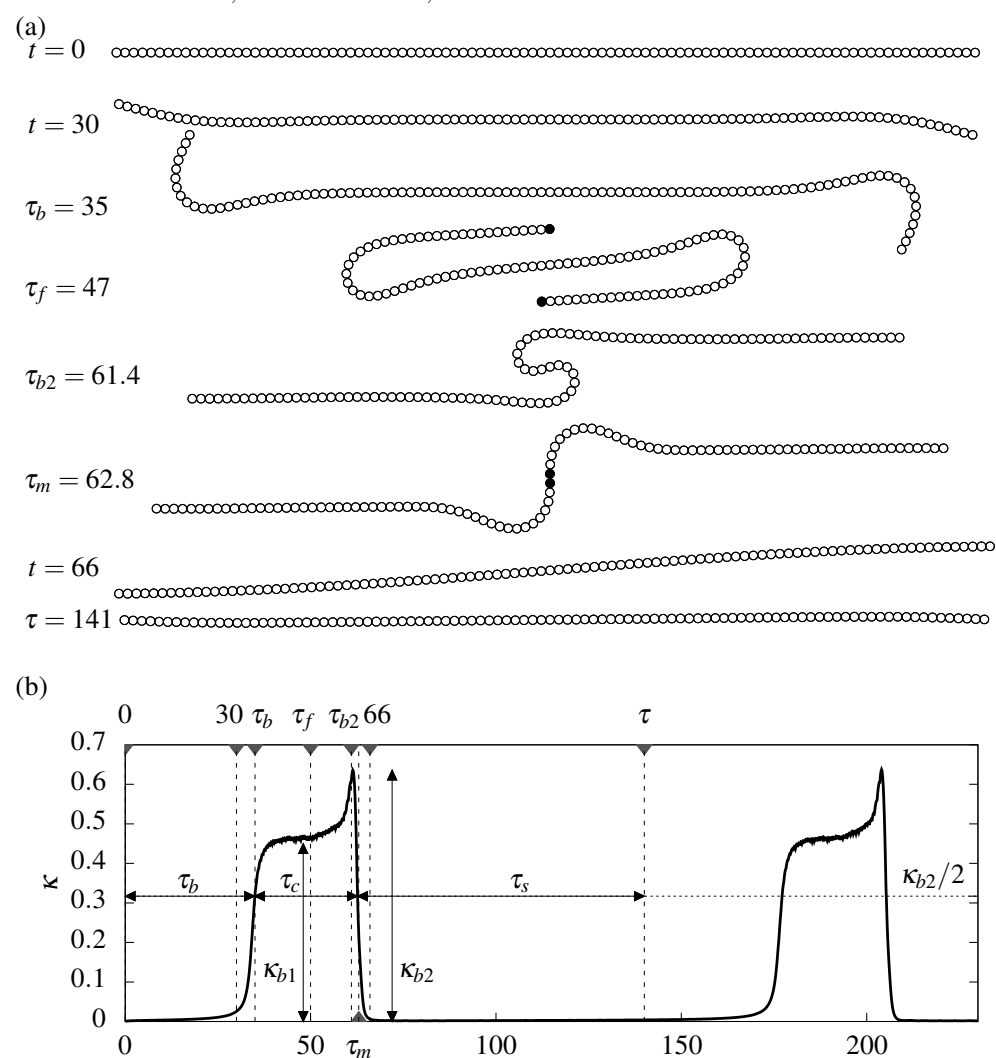


FIGURE 3. A typical evolution of the shape of a flexible fiber with aspect ratio n=100 and a moderate bending stiffness A=100 (based on the model  $\mathcal{M}_1$ ), starting from a straight fiber aligned with the flow. (a) Shapes of the fiber. The circles represent the beads actual scale along the fiber. The black circles highlight the end and middle beads during  $\tau_f$  and  $\tau_m$ . (b) Maximum local curvature  $\kappa(t)$ . Time instances corresponding to the shapes from (a) are marked with dashed vertical lines.

straightens to a position slightly tilted from the x direction at time 66, after which the fiber slowly stretches and aligns in the x direction until the end beads reach the same z coordinate at time 141.

To characterize the deformation of a fiber, an informative observable is the maximum local curvature  $\kappa(t)$  taken over the fiber length at every time instant, where similarly to the elastica model, we use lowercase symbols for the dimensionless quantities (see section 2.1). At every time t we inscribe a circle of radius  $r_{i-1,i,i+1}(t)$  on the bead centers  $\mathbf{r}_{i-1}, \mathbf{r}_i, \mathbf{r}_{i+1}$ , defining the local curvature  $\kappa_i(t) = 1/r_{i-1,i,i+1}(t)$ . The maximum local

curvature is defined as

$$\kappa(t) = \max_{2 \le i \le n-1} \kappa_i(t). \tag{3.1}$$

A typical profile of  $\kappa(t)$  obtained from the simulations is shown in figure 3(b). We identify two characteristic bending curvatures  $\kappa_{b1}$ , the value of the first plateau, and  $\kappa_{b2}$ , the maximum value over time. To characterize the shape changes, we introduce characteristic time scales:  $\tau_b$ , the bending time, then  $\tau_c$ , the curling time, and  $\tau_s$ , the stretching time, as indicated in figure 3.

Initially, for an almost straight fiber,  $\kappa(t)$  is close to 0. The rapid rise in curvature (starting around t=30) is connected with rapid bending of the ends until a characteristic curvature  $\kappa_{b1}$  is reached. We define time scale  $\tau_b$  as the time needed for a fiber to reach half of its maximum curvature  $\kappa_{b2}$  starting from a straight fiber.

After the rapid bending, a curling motion occurs. We observe the end beads passing above each other (having the same x coordinate) at a flipping time  $\tau_f = 47\dagger$ , then the kinks visible in figure 3(a) pass each other. We identify that the last event happens approximately at time  $\tau_{b2} = 61.4$ , when the curvature increases to a maximum value  $\kappa_{b2}$ . Next, there is a rapid decrease of the fiber curvature. In particular, at a turning time  $\tau_m = 62.8$  the middle beads have the same x coordinate. Later, we observe a rapid relaxation to an almost straight fiber (here at t = 66), We define time scale  $\tau_c$  as the time from the moment  $\tau_b$  when fiber reaches  $\kappa_{b2}/2$  for the first time until it reaches  $\kappa_{b2}/2$  again after passing the peak of curvature  $\kappa_{b2}$ .

After rapid relaxation, the fiber is close to straight but tilted from the flow direction. The stretching time scale  $\tau_s$  is evaluated from the time of passing  $\kappa_{b2}/2$  for the second time until the fiber ends are aligned with the flow direction again (here at time 141). Then, the motion approximately repeats itself periodically though small changes in the times identified in figure 3 are possible. Therefore, the sum  $\tau = \tau_b + \tau_c + \tau_s$  is the tumbling time scale defined as the half-period of the motion and analyzed by Słowicka et al. (2015, 2020), with typically small variations between the first tumbling and the tumblings observed at long times.

With the definitions of  $\tau_b$ ,  $\tau_c$  and  $\tau_s$  we seek to capture the time scales of the slow changes between the (much shorter) steep increase and decrease in curvature, which we consider negligible in comparison to  $\tau_b$ ,  $\tau_c$ ,  $\tau_s$ . Thus, the precise definitions of transitions points between  $\tau_b$ ,  $\tau_c$  and  $\tau_s$  can be chosen in a different way and should not have a large influence on the analysis.

We show the changes in the dynamics for different choices of n and A in figure 4. For a small A and n large enough, the end of the fiber bends multiple times and never returns to the straight state again (figure 4(a-b)), in which case  $\tau_c$  and  $\tau_s$  are not defined. Nevertheless  $\kappa$  remains approximately constant throughout most of the process. A similar qualitative picture was observed with different experimental (Forgacs & Mason 1959b; Harasim et al. 2013; Liu et al. 2018) and numerical (Nguyen & Fauci 2014; Lindström & Uesaka 2007; Liu et al. 2018; LaGrone et al. 2019) methods. The other limit is when, for a small n, A is increased to the point when the fiber bends globally along the whole length.

In the following, we will first analyze the dynamics for  $0 \le t \le \tau_b$  when the bending process originates (Sec. 4), and next we will study the shape evolution in the time range of large deformation,  $\tau_b \le t \le \tau_b + \tau_c$  (Sec. 5).

<sup>†</sup>  $\tau_f$  was called the flipping time by Słowicka *et al.* (2013, 2015) and used there to characterize the tumbling dynamics in shear and Poiseuille flows.



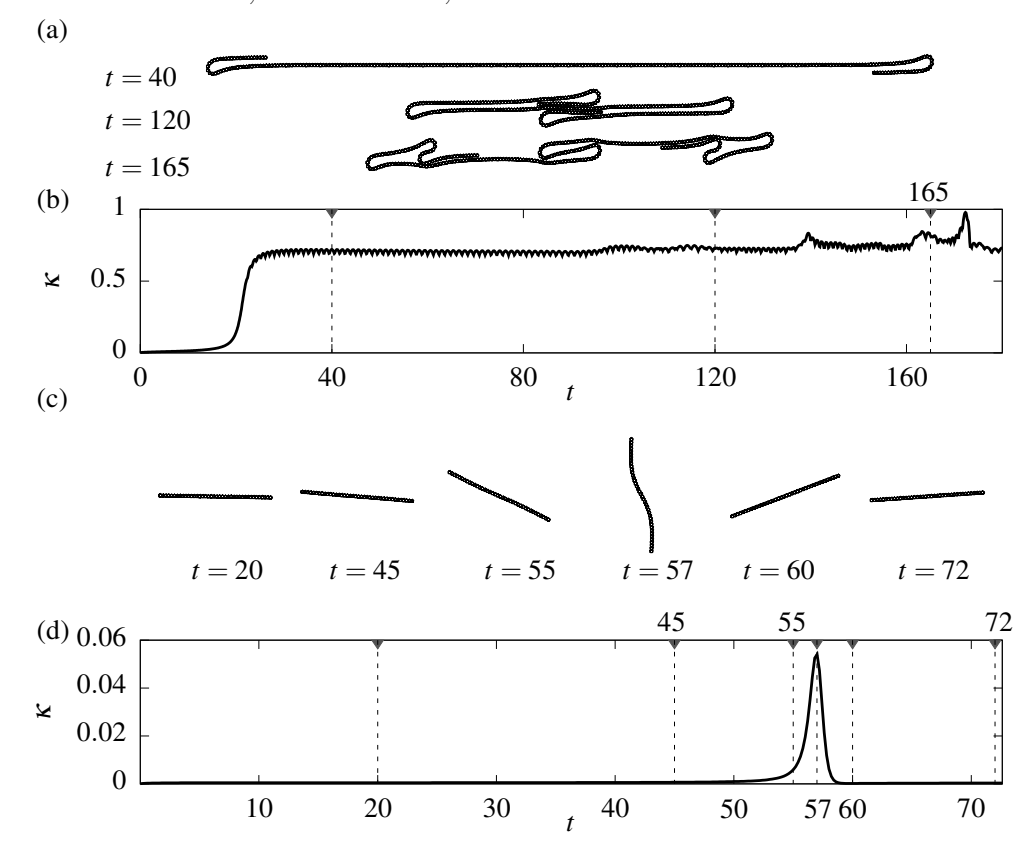


FIGURE 4. Differences in evolution of long, very flexible fibers and short, very stiff fibers (based on the model  $\mathcal{M}_1$ ). (a) Shapes of a long, flexible fiber with  $n=300,\ A=10$ . (b) Curvature of the fiber from (a) versus time. The vertical marks correspond to the shapes from panel (a). (c) Shapes of a short, stiff fiber with  $n=40,\ A=1000$ . (d) Curvature of fiber from (c). The triangle symbols with vertical dashed lines correspond to the times for which the corresponding shapes are shown in panel (c).

# 4. Bending process of initially straight fibers

#### 4.1. Bending time from numerical simulations

In addition to bending, when in a shear flow, a fiber undergoes rotation (it tumbles). It is instructive to compare the bending time  $\tau_b$ , the curling time  $\tau_c$  and the stretching time  $\tau_s$  (see figure 3) with two indicators of a fiber's rotational motion: the flipping time  $\tau_f$  and the turning time  $\tau_m$  (see figure 5(a) and the insets indicating shapes for  $\tau_f$  and  $\tau_m$ ). We find for  $A \in [1,10000)$  that  $\tau_f < \tau_m$ , which shows that the ends of the flexible fiber pass above each other earlier than the middle of the fiber rotates. As A increases, both  $\tau_m$  and  $\tau_f$  acquire the interpretation of the half tumbling time  $\tau/2$  or the quarter period  $T_J/4$  of the Jeffery orbit (Jeffery 1922), which is understood here as a periodic motion of a certain 'effective' rigid elongated object in shear flow (Słowicka *et al.* 2015, 2020) with the same period  $T_J = 2\tau$ . The period  $T_J$  of a Jeffery orbit is approximately proportional to the length of a fiber consisting of n beads (Jeffery 1922; Kim & Karrila 1991; Dhont & Briels 2007; Graham 2018).

For fibers that are very flexible or long enough (e.g., A = 10 and n = 300),  $\tau_c$  and  $\tau_s$  are not defined, because the fiber does not straighten out again (Słowicka *et al.* 2015), bending multiple times if n is sufficiently large (figure 4(a)). In the limit of very stiff

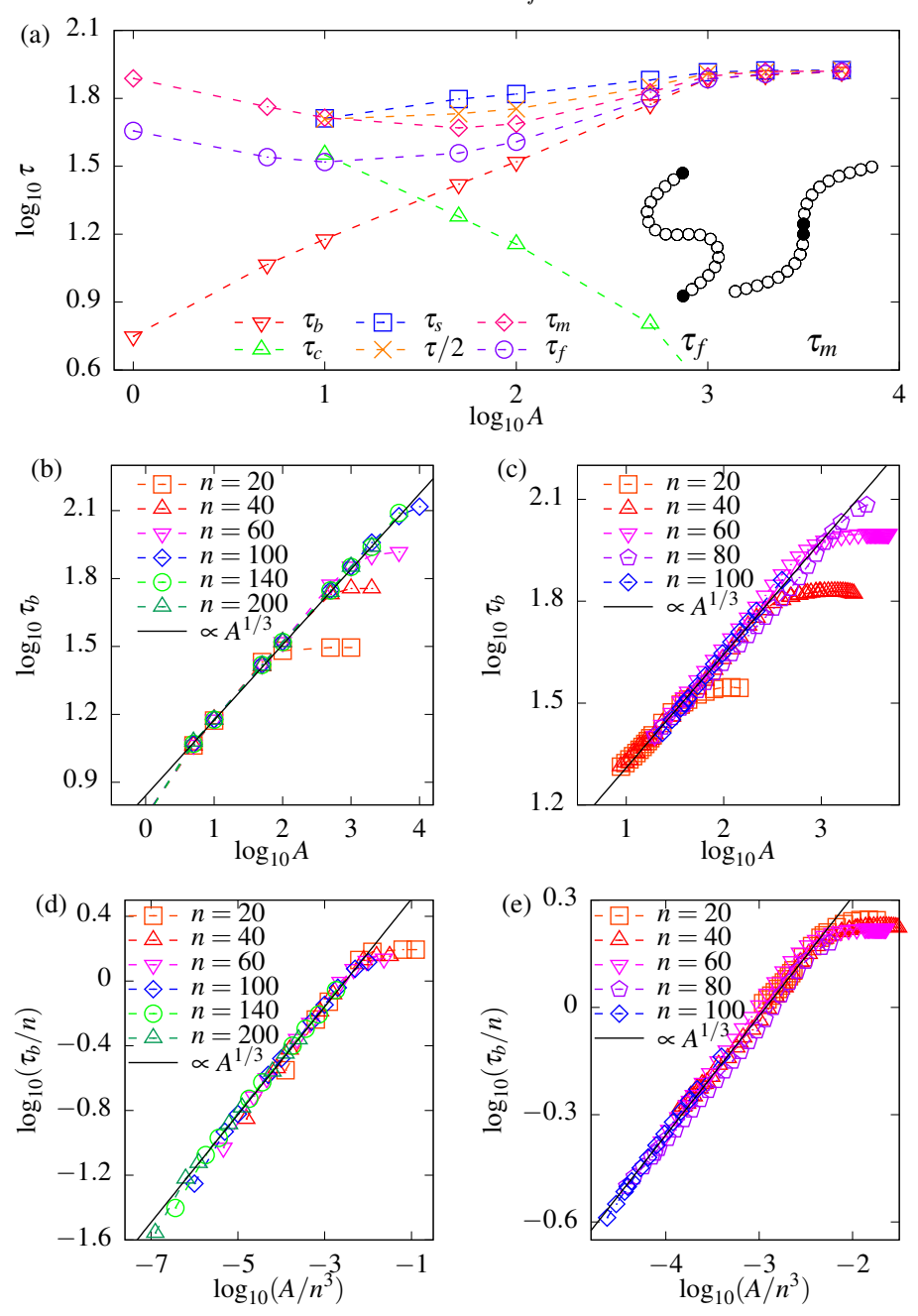


FIGURE 5. Characteristic time scales in the fiber motion. (a) Comparison of time scales of the fiber motion: the bending time  $\tau_b$ , the stretching time  $\tau_s$ , the curling time  $\tau_c$ , the flipping time  $\tau_f$  and the turning time  $\tau_m$  for n=60 and the model  $\mathcal{M}_1$ . Insets show the shapes for the times  $\tau_f$  and  $\tau_m$ . (b) and (c) Bending time  $\tau_b$  as a function of A for different n from the models  $\mathcal{M}_1$  and  $\mathcal{M}_2$ , respectively. The solid lines show  $\tau_b \propto A^{1/3}$ . In (b) the best linear fit is  $A^{0.335\pm0.002}+0.845\pm0.005$ . (d) and (e) Bending time  $\tau_b$  normalized by n is an almost universal function of  $A/n^3$ , as confirmed by the numerical data from the models  $\mathcal{M}_1$  and  $\mathcal{M}_2$ , respectively.

fibers, all the timescales defined above,  $\tau_b$ ,  $\tau_f$ ,  $\tau_m$  and  $\tau_c + \tau_s$ , converge to  $T_J/4$ , as shown in figure 5(a) for large values of A. More details about the relation between different time scales can be found in Appendix B.

The dynamics of bending change systematically as a function of A. In figures 5(b) and (c) we show  $\tau_b$  (see figure 3) as a function of A for different n, using the models  $\mathcal{M}_1$  and  $\mathcal{M}_2$ , respectively. Three regimes are visible. First, in the small A regime ( $A \lesssim 10$ ), bending dynamics are dominated by large bending angles close to the excluded volume limit. Second, for intermediate A,  $\tau_b$  does not depend on n and it follows a single power-law  $\tau_b \propto A^{1/3}$ . Third, in the regime of large A, the bending time systematically deviates from the power-law and saturates at a constant value, where larger n have larger limiting  $\tau_b$ , in agreement with  $\tau_b \to T_J/4$ .

Therefore, in figures 5(d) and (e) we replot the data from figures 5(b) and (c), respectively, using the rescaled bending time,  $\tau_b/n$ . To obtain the universal scaling, we also need to rescale the bending stiffness as  $A/n^3$ . Indeed, after such rescaling, we observe an almost universal curve in the whole range of values of n and A.

#### 4.2. A similarity solution of early times for elastical

In figures 5(b)-(e) we show the dependence  $\tau_b \propto A^{1/3}$ , which can be argued with the help of the elastica model, as we will demonstrate in this and the next section. We observe numerically that in the power-law regime the bending time does not depend on the fiber length n, which suggests an analysis based on the model of a very long fiber, initially aligned with the flow, with a tip positioned at S=0. We assume small deflections from the straight line  $\mathbf{R}=S\hat{\mathbf{e}}_x+U(S,T)\hat{\mathbf{e}}_z$ , which leads to  $K=U_{SS}$ . Further, we assume that because of small deflections,  $\hat{\mathbf{e}}_s=\hat{\mathbf{e}}_x$  and  $\hat{\mathbf{e}}_n=\hat{\mathbf{e}}_z$ . Under these assumptions we rewrite the dimensional linearized equations (2.19)

$$\dot{U}(S,T) = -\frac{EI\ln(\epsilon^{-1})}{4\pi\mu_0} U_{SSSS}(S,T) + \frac{\ln(\epsilon^{-1})}{4\pi\mu_0} F_E \delta(S), \tag{4.1a}$$

$$U(S,T) = -\frac{\ln(\epsilon^{-1})}{2\pi\mu_0} \Sigma_S(S,T), \tag{4.1b}$$

with the Dirac delta  $\delta(S)$  in the additional term that introduces the hydrodynamic force  $F_E = O(1)$ , perpendicular to the fiber axis, acting on the tip of the fiber at S = 0. This force results from the hydrodynamic interactions of the fiber beads in response to the shear flow (see section 4.3 and appendix 2.1.4). Alternatively to the delta term, the constant tip force can be formally written as a boundary condition,  $U_{SSS}(S = 0, T) = F_E/(EI)$ . We will use this approach to write equations (4.1) in the dimensionless form, corresponding to equations (2.20),

$$\dot{u} = -\frac{1}{\eta} u_{ssss},\tag{4.2a}$$

$$u = -\frac{2}{\eta}\sigma_s. \tag{4.2b}$$

In order to solve equation (4.2a) we apply boundary conditions

$$u\left(\infty,t\right)=0,\quad u_{ss}\left(\infty,t\right)=0,\quad \frac{1}{\eta}u_{sss}\left(0,t\right)=\mathcal{F},$$

$$(4.3)$$

where

$$\mathcal{F} = \frac{\ln(\epsilon^{-1})}{4} f_E \tag{4.4}$$

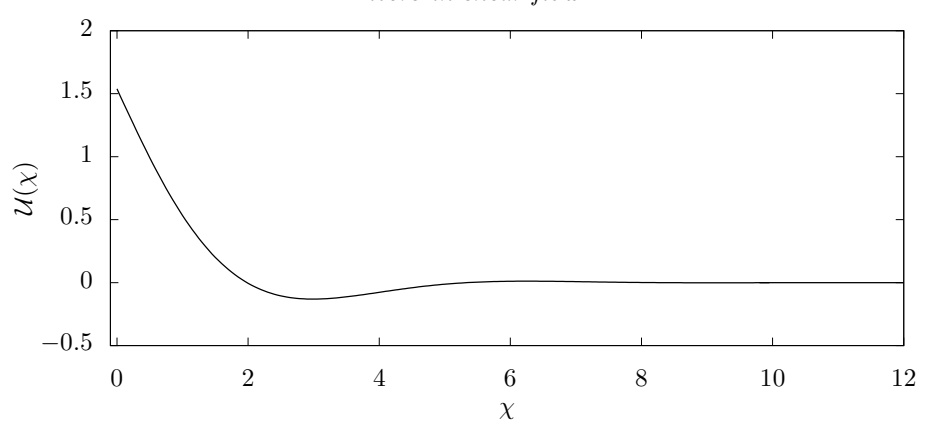


FIGURE 6. Similarity solution from the elastica model (4.7)-(4.8), valid at early times, for a fiber initially aligned with the flow.

with  $f_E = F_E / (\pi \mu_0 \dot{\gamma}(2a)^2)$ . We impose an initial condition

$$u(s, t = 0) = 0. (4.5)$$

We seek a similarity solution (Barenblatt 1996; Eggers & Fontelos 2015; Duprat & Stone 2015) and account for the forcing as

$$u(s,t) = \eta^{1/4} \mathcal{F} t^{3/4} \mathcal{U}(\chi), \text{ where } \chi = \eta^{1/4} \frac{s}{t^{1/4}},$$
 (4.6)

which leads to the equation

$$4\mathcal{U}_{\chi\chi\chi\chi} + 3\mathcal{U} - \chi\mathcal{U}_{\chi} = 0 \tag{4.7}$$

with the boundary conditions

$$\mathcal{U}(\infty) = 0, \quad \mathcal{U}_{\chi\chi}(0) = 0, \quad \mathcal{U}_{\chi\chi\chi}(0) = 1.$$
 (4.8)

The solution can be expressed with the help of special (hypergeometric) functions (e.g. use Mathematica) and the Gamma  $\Gamma(\cdot)$  function

$$\mathcal{U}(\chi) = \frac{\chi^3}{6} - \frac{2\chi_1 F_3\left(-\frac{1}{2}; \frac{1}{2}, \frac{3}{4}, \frac{5}{4}; \frac{\chi^4}{256}\right)}{\sqrt{\pi}} + \frac{\sqrt{2}_1 F_3\left(-\frac{3}{4}; \frac{1}{4}, \frac{1}{2}, \frac{3}{4}; \frac{\chi^4}{256}\right)}{\Gamma\left(\frac{7}{4}\right)}.$$
 (4.9)

The function  $\mathcal{U}(\chi)$  is shown in figure 6. From  $\mathcal{U}(\chi)$  we calculate

$$u(s,t) = \mathcal{F}\left(\frac{\eta s^3}{6} - \left(\frac{4\eta t}{\pi}\right)^{1/2} s_1 F_3\left(-\frac{1}{2}; \frac{1}{2}, \frac{3}{4}, \frac{5}{4}; \frac{s^4 \eta}{256t}\right) + \frac{16\eta^{1/4}}{3\pi} t^{3/4} \Gamma\left(\frac{5}{4}\right) {}_1 F_3\left(-\frac{3}{4}; \frac{1}{4}, \frac{1}{2}, \frac{3}{4}; \frac{s^4 \eta}{256t}\right)\right). \tag{4.10}$$

This result can be expanded around s = 0

$$u(s,t) = \mathcal{F}\left(\frac{16\eta^{1/4}t^{3/4}}{3\pi}\Gamma\left(\frac{5}{4}\right) - s\left(\frac{4\eta t}{\pi}\right)^{1/2} + \frac{\eta s^3}{6} + \dots\right)$$
(4.11)

and, in particular at s=0, the end moves according to

$$u(0,t) = (\eta t^3)^{1/4} \mathcal{F} \frac{16\Gamma(\frac{5}{4})}{3\pi}.$$
 (4.12)

The complete solution of the similarity ansatz has the magnitude of the deflection  $u(0,t) \propto (\eta t^3)^{1/4}$ . The length scale on which the deflection occurs is  $s \propto (t/\eta)^{1/4} \propto (u(0,t)/\eta)^{1/3}$ . In time the "height" of the deflection grows more rapidly than its "width", which makes the tip more and more steep. The bending stiffness has an opposite effect and makes the deformation less steep with increasing  $A \propto \eta^{-1}$ .

#### 4.3. Comparing the numerical simulations with the similarity solution

In this section, we present results from the numerical simulations based on the model  $\mathcal{M}_1$  and compare them with the predictions from the elastica model. According to the elastica similarity solution, the fibers have features of the shape that follow the scaling laws with t and  $\eta$  presented above. Therefore, we analyze the z coordinate of the relative position of the first bead at time t with respect to its initial position,  $z_1(t) = \hat{\mathbf{e}}_z$ .  $(\mathbf{R}_1(t) - \mathbf{R}_1(0))$ , which is calculated from the bead-spring simulations  $\mathcal{M}_1$  (figure 7(a)). We show the same data with the rescaled time  $t/A^{1/3}$  in figure 7(b). This scaling is suggested by the elastica model, if we identify the height  $z_1(t)$  of the fiber end with the deflection of the elastica tip u(0,t), given by equation (4.12), and we remind that  $\eta \propto 1/A$ . We also fit a straight line to the numerical values of  $\log_{10} z_1(t)$  as a function of  $\log_{10}(t/A^{1/3})$ , in the linear region  $\log_{10}(t/A^{1/3}) < -1$ , where deformations are still small and no deviations from the power law are observed. While fitting, we used data from all the simulations where  $n \ge 60$  and  $A \ge 50$ . The calculated slope 0.787 is very close to 3/4 theoretically predicted from the dynamics of elastica. In order to further compare simulations with the theoretical results we will use the best fit of the tip height in the form  $z_1(t) = C(t/A^{1/3})^{3/4}$ , which is suggested by the elastica, that results with  $C \approx 10^{-0.81}$ .

In figure 7(c) we present the numerical shapes of the fibers with different A and n taken at different times but still within the range of the similarity solution, with  $t/A^{1/3} \lesssim 10^{0.6} \approx 4$ . The ends of these shapes can be to a certain extend superimposed onto each other by scaling the coordinates as  $\tilde{x} = x/(tA)^{1/4}$  and  $\tilde{z} = z/(t^3/A)^{1/4}$ , respectively, in accord with predictions from the elastica, and translating by a shift  $x_0$ , which is different for each fiber, as shown in figure 7(d). The rescaled shapes are plotted together with two plots of the similarity solution as a function  $a_k \mathcal{U}(\tilde{x}b_k)$ , k = I, II, which correspond to our two different approaches to compare the hydrodynamic forces,  $f_{H1}$  and  $f_E$ , exerted on the fiber tip in the bead (Sec. 2.1) and elastica (Sec. 4.2) models, respectively. (Actually, we will be comparing the limiting value  $f_H$  for  $n \to \infty$  rather than  $f_{H1}$ .)

In both approaches, we assume the identical tip heights  $z_1(t)$  and u(0,t) in the bead and elastica models, respectively. In the first approach (I), both forces are assumed to be the same,  $f_H = f_E$ . Therefore,  $\mathcal{F}$  is related to  $f_H$  by equation (4.4). On the other hand,  $\eta \approx 4/(A \ln \epsilon^{-1})$ , as shown below (2.21), and equation (4.12) links  $\mathcal{F}$  to the height  $u(0,t) = z_1(t)$  of the fiber. Using the numerical fit of  $z_1(t)$ , shown in figure 7(b), we find  $\mathcal{F}$ , and from this result, using equation (4.4) we determine the magnitude  $f_E$  of the dimensionless tip force in the elastica model. The approach (I) is given by the following equations,

$$\mathcal{F} = 10^{-0.81} \frac{3\pi (\ln \epsilon^{-1})^{1/4}}{16\Gamma(\frac{5}{4})\sqrt{2}} \approx 0.071 (\ln \epsilon^{-1})^{1/4}, \tag{4.13}$$

$$f_E = 0.284(\ln \epsilon^{-1})^{-3/4} = f_H \approx 0.16,$$
 (4.14)

$$\eta \approx 4/(A \ln \epsilon^{-1}).$$
(4.15)

From equation (4.14) we find  $\epsilon^{-1} \approx 9$ , which is rather far from typical aspect ratios used in the numerical simulations. We use the above values to compare shape of the fiber made

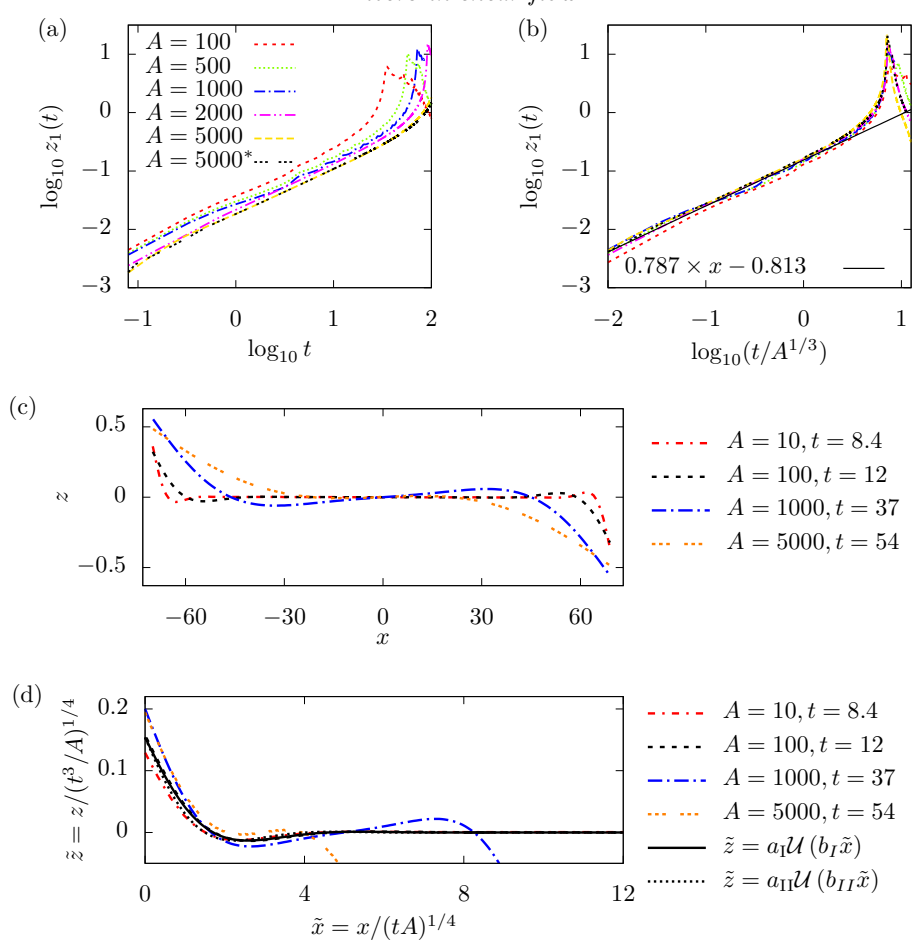


FIGURE 7. Scalings in the numerical simulations for small deflections. (a) Height  $z_1(t)$  of the fiber tip above the horizontal line passing through the center of the fiber (from the  $\mathcal{M}_1$  model). Fibers have n=100, except the fiber denoted with \* that has n=140. (b) Height  $z_1(t)$  from panel (a) as a function of the rescaled time  $t/A^{1/3}$  (in log-log scale). The red line comes from a fit to all  $\mathcal{M}_1$  data with  $n \geq 60$ ,  $A \geq 50$  for times  $t/A^{1/3} < 0.1$ . (c) Shapes of fibers from the bead model  $\mathcal{M}_1$  for n=140 and different A at arbitrarily chosen times at the end of the regime of the similarity solution. (d) Shape of fibers from the panel (c), scaled according to the similarity solution  $z_1(t) \approx u(s,t)$ , with u given by equation (4.6), and translated to approximately overlay the left ends. The numerically obtained shapes are superimposed onto theoretically calculated shapes  $a_k \mathcal{U}(\tilde{x}b_k)$ , k=1, II, with  $\mathcal{U}$  given by equation (4.9) and the coefficients  $a_k$ ,  $b_k$  given in terms of  $\mathcal{F}$  and  $\eta$  which result from approaches I and II to compare between the bead model and the elastica, given in equations (4.13)-(4.15) and (4.16)-(4.17), respectively.

of beads with the elastica. Starting from eq. (4.6) we find that  $a_{\rm I} = 0.1$  and  $b_{\rm I} = 1.16$  and plot the corresponding elastica shape (solid line) in figure 7(d).

In the second approach (II), we assume that velocities of the fiber segments are the same in the bead and elastica models. In this way, mobilities times forces are equal to each other. The mobility for the elastica comes from the slender body theory, while in the equations of motion for a fiber made of beads, there appear the single-sphere Stokes

mobility. Therefore in approach (II), we match the elastica and bead quantities as follows,

$$\mathcal{F} \equiv \frac{\ln(\epsilon^{-1})}{4} f_E = \frac{1}{3} f_H, \tag{4.16}$$

$$\eta = \frac{3}{A}.\tag{4.17}$$

Then, using the numerical results, from equation (4.12) we obtain

$$f_H = 10^{-0.81} \frac{9\pi}{16\Gamma(5/4)3^{1/4}} \approx 0.23,$$
 (4.18)

which is not very far from the numerical value  $f_H = 0.16$  obtained for large n. In this approach the parameter  $\epsilon^{-1}$  is not used at all. With the use of this set of values and eq. (4.6) we find that  $a_{\rm II} = 0.1$  and  $b_{\rm II} = 1.32$ . We plot the corresponding elastica shape (dotted line) in figure 7(d).

#### 4.4. At early times beyond small deformations

In this section, we will focus on an early phase of bending for times  $t \lesssim \tau_b$ . We will analyze the simulations with the bead model  $\mathcal{M}_1$  and compare them with the scaling laws following from the elastica model. In the early phase, a flexible fiber aligned with shear flow slowly starts to bend its ends while the middle part of the fiber remains straight. The characteristic length scale of the deformed fiber segments at both ends remains approximately constant in time until a significant, rapid bending is developed at the bending time  $\tau_b$ , associated with a fast increase of both the local curvature  $\kappa$  (figure 3(b)) and the tip deflection  $z_1(t)$  along z (figure 7(a,b)). A corresponding sequence of consecutive fiber shapes, found numerically with the model  $\mathcal{M}_1$ , is shown in figure 8. The significant bending from the middle to the last shape occurs at a very short time scale.

In figure 3(b), the bending time  $\tau_b$  was defined as the time when the maximal local fiber curvature reaches one half of its largest value,  $\kappa(\tau_b) = \kappa_b/2$ . We now add a physical interpretation: at a time close to  $\tau_b$ , the deflection  $z_1(t)$  of the fiber tip approaches the first local maximum, visible in figures 7(a,b). The corresponding fiber shape at  $t = \tau_b$  is shown in figure 8 as the last one.

The linear regime of small deformations is limited to short times. For example, in figure 8, all shown fibers are already beyond this regime. However, to understand the dynamics in the early phase, it is worthwhile to begin the analysis from the linear regime where the universal scaling of shapes follows directly from the self-similar solution, specified by equations (4.6) and (4.9). One of characteristic features of the self-similar solution is that the same deflection  $z_1(t) = u(0,t)$  of the fiber tip is reached at the same rescaled time  $tA^{-1/3} \propto t\eta^{1/3}$  (and with the same rescaled length  $sA^{-1/3}$  along the fiber). The numerical results shown in figure 7(b) illustrate that  $z_1(t)$  is determined by  $tA^{-1/3}$  not only in the range of small deformations, but also beyond it. The tip deflection  $z_1(t)$  remains a universal function of  $tA^{-1/3}$  until its argument reaches value slightly smaller than, but very close to  $t_{\rm max}A^{-1/3} \approx 7.2$ , with  $t_{\rm max}$  defined as the time when  $z_1$  has a local maximum  $u_{\rm max}$ . In the log-log scale, as shown in figure 7(b), the universal curve is close to a straight line for  $tA^{-1/3} \lesssim 4$  (in the linear regime). For  $tA^{-1/3} \gtrsim 4$ , a significant deviation from the straight line is observed caused by nonlinear effects.

The deviations from the linear regime in the numerical simulations can be interpreted by the elastica evolution in the range where the nonlinear terms in eqs. (2.20) become important, i.e.,

$$\kappa_{ss} \sim \sigma \kappa.$$
(4.19)

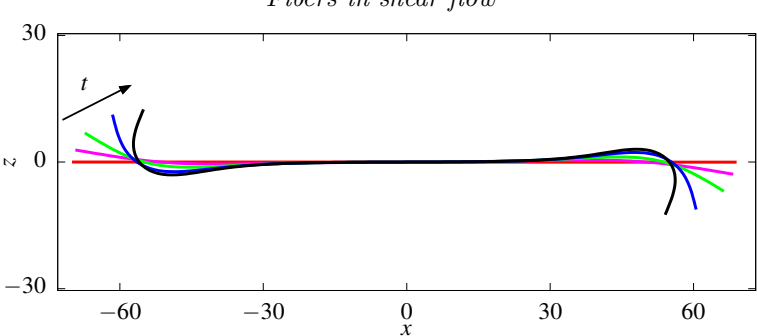


FIGURE 8. A typical evolution of shapes of a flexible fiber in an early stage of bending. Here n=140 and A=1000. The consecutive time instants shown are t=50, 66, 69, 70, 70.5, with the last one approximately equal to  $\tau_b$ .

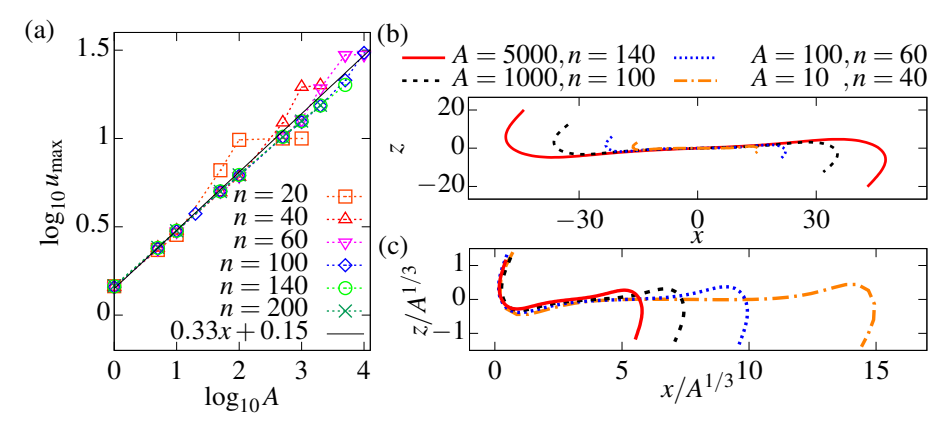


FIGURE 9. Maximum deflection  $u_{\text{max}}$  of the fiber tip, defined as  $z_1(t_{\text{max}})$  at the time  $t_{\text{max}}$  of the first maximum, evaluated numerically from the bead model  $\mathcal{M}_1$ . (a)  $u_{\text{max}}$  as a function of A for different n, with the approximate scaling  $\propto A^{1/3}$ . (b) Shapes of fibers at  $t_{\text{max}}$  for different A and A. (c) Rescaled shapes of fibers from (b), translated to overlay the bending left ends.

Next, we observe that the change in the elastica dynamics occurs away from the small deflection state so we can use the relation (4.2b), which implies the scaling,

$$\sigma \sim \eta u s$$
 (4.20)

with the results from similarity solution to show that

$$O(1) = O(\sigma s s) = O(\eta u s^3) \approx \eta^{1/2} t^{3/2} \Rightarrow O(1) = \eta t^3. \tag{4.21}$$

As  $\eta \propto A^{-1}$ , these balances suggest that the time scale  $\tau_b$ , when the nonlinear terms become important, follows the power law  $\tau_b \propto A^{1/3}$ , which is in a good agreement with results presented in figure 5(b-e).

For times close to  $\tau_b$  and  $t_{\rm max}$ , the tip deflection  $z_1(t)$  leaves the universal curve, as shown in figure 7(a,b), and the maximum deflection  $u_{\rm max}$  depends on A. We observe that in the range of A, in which the evolution follows a power law,  $u_{\rm max} \propto A^{0.33}$ , as determined numerically from the bead model  $\mathcal{M}_1$  and shown in figure 9(a). This scaling might reflect a memory of the initial phase of the fiber movement as analyzed using the elastica. A linearly deflected fiber changes its shape over a length scale  $s \propto A^{1/4}t^{1/4}$  and time scale  $t \propto A^{1/3}$  (equation (4.6)) thus, we find that  $s \propto A^{1/3}$  at time t. However, as illustrated in figure 8, for early times  $t \lesssim \tau_b$ , the typical length scale of bending remains

almost constant in time, what allows to expect that  $u_{\text{max}} \propto A^{1/3}$ . The numerical results suggest that during the rapid bending the scaling in the x direction becomes comparable to the scaling in the z direction. To demonstrate this feature, we collect several fiber shapes for different values of n and A, at times  $t_{\text{max}}$  of the maximum deflection (figure 9(b)), and we replot them in figure 9(c) by rescaling both axes by  $A^{1/3}$ , which allows for the approximate overlapping of the shapes after translating them in the x direction.

The scalings with  $A^{1/3}$ , typical for the early phase of the bending process, do not depend on n. For  $t \lesssim \tau_b$ , bending of the fiber ends is a local process. However, the typical bending length scale increases with A, and therefore for a larger stiffness, the scalings are satisfied by a sufficiently long fiber only.

### 5. Highly bent fiber

#### 5.1. Bead model simulations

We now move on to discuss the dynamics for times  $\tau_b \lesssim t \lesssim \tau_b + \tau_c$ , when the fiber is significantly bent, with the maximum local bending curvature  $\kappa_{b2}/2 \leqslant \kappa(t) \leqslant \kappa_{b2}$ , where  $\kappa_{b2}$  is the largest maximum local curvature during this time period (see figure 3). In this range, the main feature of the dynamics is its maximum local curvature  $\kappa(t)$ . Therefore, we first discuss if (and how) the characteristic features of the dynamics depend on a specific choice of the time instant when the curvature is determined.

In figure 3(b) we have illustrated that there exists a typical plateau of the curvature,  $\kappa_{b1}$ , and the largest value  $\kappa_{b2}$ . Comparison with figures 4(b) and (d) indicates that both values vary systematically with A. We analyze this dependence in figure 10(a). On a loglog plot,  $\kappa_{b1}$  is systematically below  $\kappa_{b2}$ , and the inset (for n = 140) illustrates that the ratio  $\kappa_{b1}/\kappa_{b2}$  slowly decays with increasing A, but this effect is not large. The numerical data shows that over a few decades of A, the ratio  $\kappa_{b1}/\kappa_{b2}$  changes only by 30%, and it tends to  $\kappa_{b1}/\kappa_{b2} \sim 0.7$  for large A. This observation suggests that  $\kappa_{b2}$  depends on A in a similar way as  $\kappa_{b1}$ . The fiber is first in the state of a typical bend and tightens to a maximum curvature for a short time afterwards. However, the plateau in the  $\kappa(t)$  that allows determination of  $\kappa_{b1}$ , for a given n, occurs only for a finite range of A, while  $\kappa_{b2}$  is well defined for any value of A. For example, in case of n = 40, in figure 10(a) there are no data points above A = 100 indicating  $\kappa_{b1}$  while for n = 140,  $\kappa_{b1}$  can be observed up to A = 2000. Therefore, in the following we will focus on the analysis of  $\kappa_{b2}$ .

Depending on the values of A, three regimes of fiber bending can be identified, as shown in figures 10(b,c) for the bead models  $\mathcal{M}_1$  and  $\mathcal{M}_2$ , respectively. The schematics in figure 10(b) show three typical fiber shapes with n=20 for each of the regimes. First, in the regime of a very flexible fiber  $(A \leq 10)$ , the maximum curvature is close to the excluded volume (EV) of the beads, with  $\log_{10} \kappa_{b2} \leq \log_{10}(\sqrt{3}) \approx 0.24$ , which is independent of n. Second, there is a regime  $A \geq 10$ , where  $\kappa_{b2}$  as a function of A continues with a power-law dependence until it deviates from the slope, which happens for different A depending on n. The larger n, the larger range of A that exhibit the power-law dependence. Inside this regime, for a given A, all fibers that are long enough have the same  $\kappa_{b2}$ , which is independent of n. We interpret this response as local bending. Third, there is a large A regime, which starts after  $\kappa_{b2}$  departs from the power law. This corresponds to  $\kappa_{b2}^{-1}$  comparable to or larger than the fiber length, which we interpret as global bending. This classification of  $\kappa_{b2}$  is valid even for very long fibers (having multiple loops), and also for very stiff ones (with no pronounced plateau of the fiber curvature  $\kappa(t)$ ). For each n, the regimes of A where the power laws are observed for  $\kappa_{b2}$  agree with the corresponding

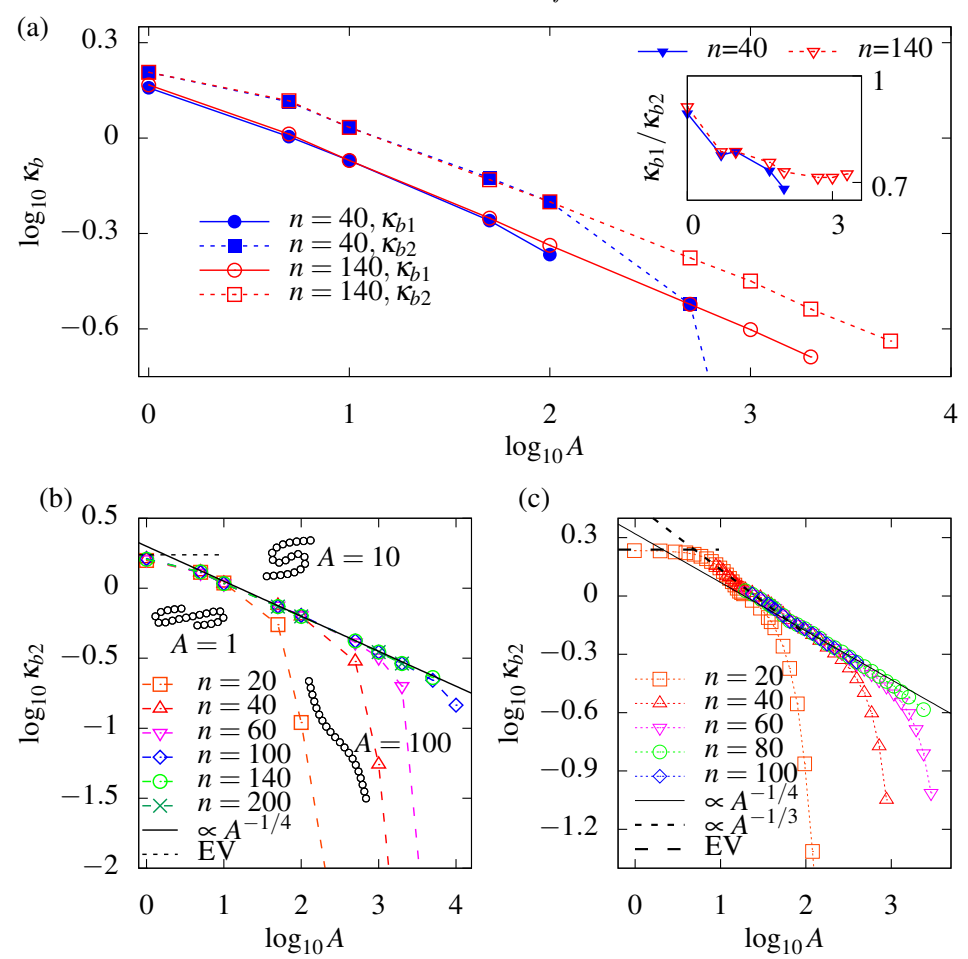


FIGURE 10. Fiber bending curvature as a function of A, evaluated from the bead models. (a) Difference between typical  $\kappa_{b1}$  and maximum  $\kappa_{b2}$  curvatures for two different lengths of fiber (n=40 and n=140), based on the model  $\mathcal{M}_1$ . The inset shows the ratio of bending curvatures  $\kappa_{b1}/\kappa_{b2}$  as a function of n. (b) and (c) Scaling of the maximum curvature  $\kappa_{b2}$  as a function of A, for different n, determined from the models  $\mathcal{M}_1$  and  $\mathcal{M}_2$ , respectively. The solid lines corresponds to  $\kappa_{b2} \propto A^{-1/4}$ , the dashed inclined line show  $\kappa_{b2} \propto A^{-1/3}$ , and the horizontal dashed lines show the curvature based on excluded volume (EV). The schematics in (b) show the shape of a fiber with n=20 for A=1,10 and 100.

regimes identified for  $\tau_b$  (compare the ranges of A in figures 10(b,c) with the ranges in figures 5(b,c), respectively).

Comparison of figures 10(b) and 10(c) indicates that if the bending stiffness ratio A is not very small ( $A \gtrsim 10$ ) and not too large (with the upper bound dependent on n), the power-law scalings of  $\kappa_{b2}$  predicted by the  $\mathcal{M}_1$  and  $\mathcal{M}_2$  models are in a reasonable agreement with each other, and the curves only weakly depend on n. However, for  $10 \lesssim A \lesssim 100$ , the maximum curvature  $\kappa_{b2}$  in the  $\mathcal{M}_2$  model decays more rapidly with A than in  $\mathcal{M}_1$ , with approximately  $\kappa_{b2} \propto A^{-1/3}$  rather than  $\kappa_{b2} \propto A^{-1/4}$ , respectively (for the  $\mathcal{M}_1$  model,  $\kappa_{b2} \propto A^{-0.253\pm0.003}$  as determined numerically). For  $A \lesssim 10$ , the maximum curvature  $\kappa_{b2}$  determined from the  $\mathcal{M}_2$  model saturates at the excluded volume value while in model  $\mathcal{M}_1$  this effect is seen for more flexible fibers with  $A \lesssim 1$ . Although the treatment of hydrodynamic interactions is more precise within the bead model  $\mathcal{M}_2$ , it

seems that the main reason for some differences between the maximum bending curvature  $\kappa_{b2}$  obtained by the  $\mathcal{M}_1$  and  $\mathcal{M}_2$  models is the use of different expressions for the bending potential energy, as discussed in detail in Appendix B.

#### 5.2. Comparing with the elastica model

We are going to show now that the scaling of the fiber maximum curvature  $\kappa_b \propto A^{-1/4}$ , independent of n and characteristic for the local bending, can be argued with the elastica model (2.20). We propose that in the local bending process there is only one length scale  $\kappa_b^{-1}$  representative of the deformed fiber. It is consistent with the models of Harasim et al. (2013); LaGrone et al. (2019); Liu et al. (2018) and with our findings that  $\kappa(t)$  is in the curling motion close to a typical constant value  $\kappa_{b1}$ .

Next, from the linearity of shear flow, we argue that the magnitude of the flow velocity incident on the fiber and the fiber velocity scale linearly with the length scale  $(\hat{\mathbf{e}}_x(\hat{\mathbf{e}}_z \cdot \mathbf{r}) - \dot{\mathbf{r}}) \propto \kappa_b^{-1}$ . Comparing the magnitudes of terms in (2.20b), we find that the dimensionless tension scales as

$$\sigma \propto \eta \kappa_b^{-2} + \kappa_b^2. \tag{5.1}$$

This dependence together with (2.20a) gives

$$\eta \kappa_h^{-1} \propto \kappa_h^3 + \left(\eta \kappa_h^{-2} + \kappa_h^2\right) \kappa_b,\tag{5.2}$$

resulting in  $\kappa_b \propto \eta^{1/4} \propto A^{-1/4}$ . It is also true that  $\sigma \propto A^{-1/2}$  and  $\sigma_s \propto A^{-3/4}$ . Note that these arguments apply to the maximum curvature in the whole range of the curling motion with a large shape deformation, in particular for  $\kappa_b = \kappa_{b1}$  and  $\kappa_b = \kappa_{b2}$ .

The scalings obtained from the elastica model can be compared with the results from the bead-spring simulations with the model  $\mathcal{M}_1$ . The force  $\mathbf{F}_i$  acting on each bead i as the result of the elastic constitutive laws can be decomposed into the force components normal  $N_i$  and tangential  $T_i$  to the fiber centerline. In figure 11(a) we show shapes of locally bent fibers with n = 100 for three different values of A. The color-coded representations of  $N_i$  and  $T_i$  are included in the following way. Each bead is depicted by a hemisphere, which has an orientation that indicates the direction of  $T_i$  (inset), while the color coding shows the ratio of the magnitudes of forces normal and tangential to the fiber,  $|\mathbf{N}_i|/|\mathbf{T}_i|$ . In order to compare the simulation data quantitatively with the scalings deduced above from the elastica, it is sufficient to choose any time from the curling motion of the fiber. As we compare between different A, we introduce the transformation of the bead numbering  $i' = (i - i_0)A^{-1/4}$  (i is a discrete analog of the arc length s), where a shift  $i_0$  is chosen (for each fiber separately) to overlap the extrema. In the figures 11(b,c) we show the profile of local curvature  $\kappa_i$  over half of the fiber (i=1...50) for the shapes presented in figure 11(a). In figure 11(b) the raw data is plotted and in figure 11(c)  $\kappa_i$ is multiplied by  $A^{1/4}$  to show the scaling suggested by the elastica model. From the bead-spring simulations we have direct access to  $\mathbf{T}_i \cdot \hat{\mathbf{e}}_s$  acting at the center of bead i, which is the analog of the derivative of the tension  $\sigma_s(s)$  for the elastica.  $\mathbf{T}_i \cdot \hat{\mathbf{e}}_s$  is shown in figure 11(d), and in figure 11(e) we demonstrate that the tangential forces scale as  $A^{-3/4}$ , which has been also suggested by the elastica model.

#### 5.3. Curling velocity and curling time

In section 3 we introduced the curling motion and the associated curling time  $\tau_c$  (see figure 3). During the curling motion, the first bead travels from left to right approximately over the distance L=2na with respect to the fiber's center. Snapshots illustrating the shape evolution are shown using the schematics at the top of figure 12(a) for the fiber with n=100 and A=100. We define the curling velocity  $v_x(t)$  as the x-component of the

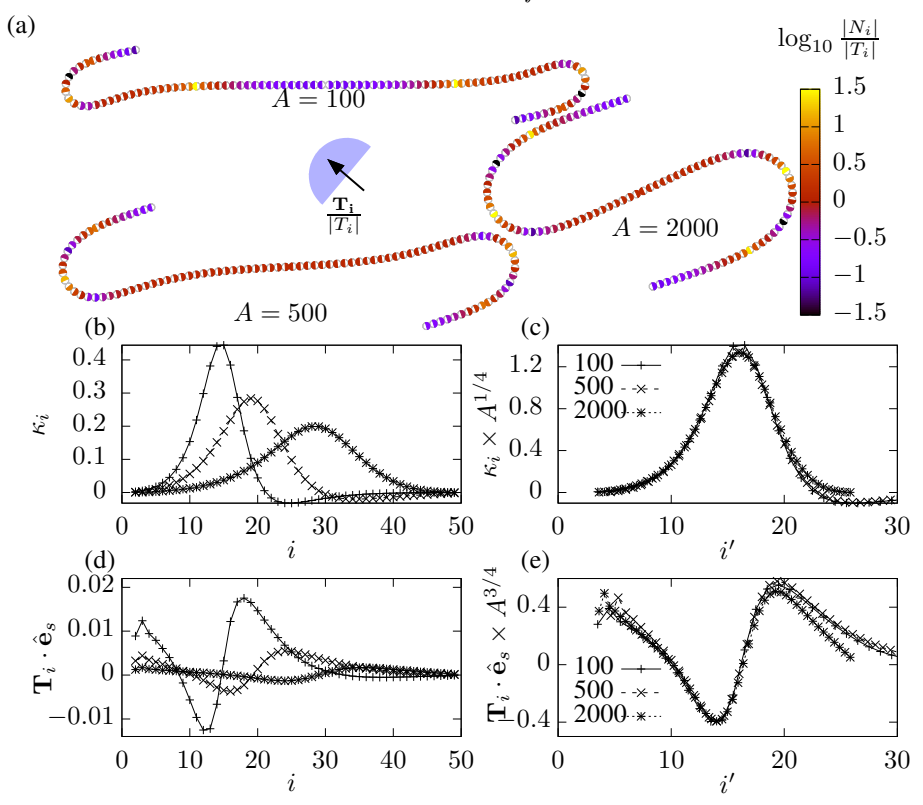


FIGURE 11. Instantaneous distribution of forces and curvatures on individual beads (fiber statics) for three locally bent fibers with n=100 and A=100,500,2000. (a) Shapes of the fibers. The color coding shows the ratio of the normal  $|\mathbf{N}_i|$  to the tangential  $|\mathbf{T}_i|$  force components acting on each bead i, represented as a hemisphere. The orientation of hemispheres shows the direction of  $\mathbf{T}_i$ . (b) Curvature  $\kappa_i$  on bead i along the fiber. (c) Rescaled curvature as a function of rescaled position  $i' = (i - i_0)A^{-1/4}$  along the fiber. (d) Tangential forces  $\mathbf{T}_i \cdot \hat{\mathbf{e}}_s$  acting on beads i - the discrete analog of the tension's derivative  $\sigma_s$  for the elastica. (e) Rescaled  $\mathbf{T}_i \cdot \hat{\mathbf{e}}_s$  as a function of i'.

velocity of the first bead. At the bottom of figure 12(a), we plot  $v_x$  versus time, for the fibers with A=100 and different values of n. Initially,  $v_x$  is close to zero. Then, it rises significantly and we observe the first peak, the plateau and the second peak. Numerical simulations show that for a given A, the profile of  $v_x(t)$  in the initial phase of the motion is almost the same for different n. In figure 12(a), the plots of  $v_x(t)$  for different n are almost superimposed for a long time. The changes between  $v_x(t)$  with different n occur when the fiber stops to undergo curling motion due to its limited length. The peaks of  $v_x$  are observed at the times of the steepest changes in  $\kappa(t)$ , as illustrated in figure 12(b). The first peak takes place at the time close to the bending time  $\tau_b$ , and the second one approximately after the curling time  $\tau_c$  (compare with figure 3). Therefore, our definitions of  $\tau_b$  and  $\tau_c$  seem to well separate three different phases of the fiber dynamics.

We have found empirically that  $\tau_c$  as a function of A and n can be collapsed on a single universal line when plotted versus  $A/n^{3.5}$ , as shown in figure 12(c). For small values of  $A/n^{3.5}$ , the curling time  $\tau_c$  tends to a power law with the exponent -1/3, as determined empirically. Thus we observe that in the limit of long fibers, we can approximate the curling time as  $\tau_c \propto A^{-1/3} n^{1.17}$ . That is,  $\tau_c$  is almost linear in n. The deviations might be related to a larger average resistance during the curling motion of longer fibers. Indeed,

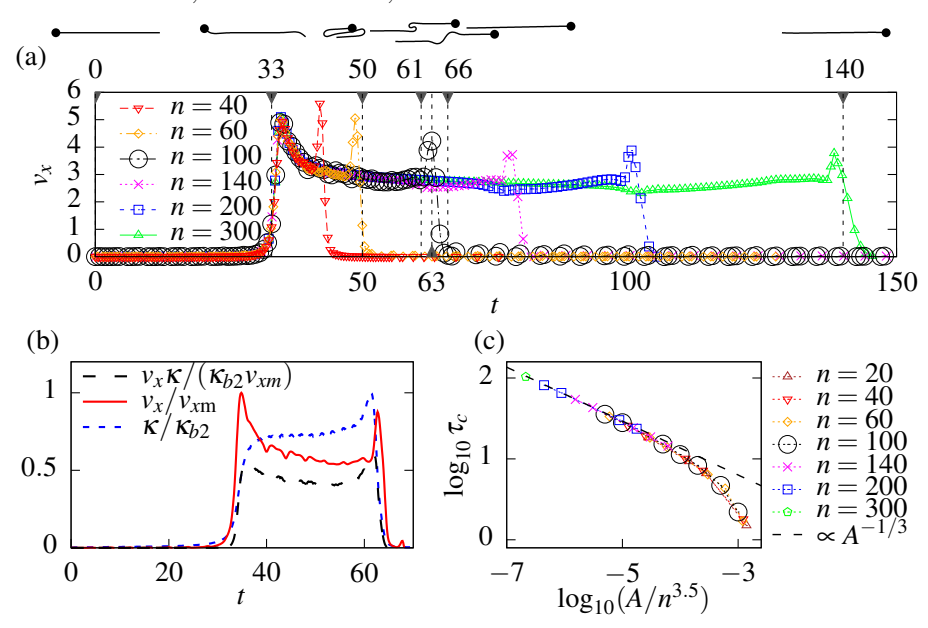


FIGURE 12. The curling motion. Results from the bead model  $\mathcal{M}_1$ . (a) The x component  $v_x$  of the first bead velocity as a function of time for A=100 and different aspect ratios n. The enlarged black circles represent the fiber of aspect ratio n=100 (shown in figure 3). The schematics above the plot show the shapes for n=100 at times marked with vertical dashed lines; the first bead is marked with a dot. (b) Comparison of  $v_x(t)$  (normalized with the maximum observed value  $v_{xm}$ ) with  $\kappa(t)$  (normalized with the maximum curvature  $\kappa_{b2}$ ), for A=100 and n=100. (c) Scaling of the curling time  $\tau_c$  as a function of  $A/n^{3.5}$ , found empirically.

figure 12(a) illustrates that for longer fibers, the contribution to the average curling velocity from the initial and final peaks is smaller, and therefore the average curling velocity is smaller, which leads to the curling time increasing with n a little faster than linearly.

The dynamics analogous to the curling motion was investigated in the literature experimentally, numerically and by the elastica model, with and without the Brownian motion (Forgacs & Mason 1959b; du Roure et al. 2019). We have shown here that on the onset of curling motion the characteristic length scale ( $\propto A^{1/3}$ ) is different from the one observed later in the highly bent state ( $\propto A^{1/4}$ ), which leads to the analogous scalings for  $v_x$  at earlier and later times, respectively. Therefore we emphasize the importance of the time evolution during the curling motion but at the same time we benefit from the previous studies of Harasim et al. (2013); Liu et al. (2018) who reported the linear dependence between the local radius of curvature of the bent tip and its track velocity (analogous to our curling velocity), both approximately constant in time.

We have found that in the regime of the local bending, during the curling motion, the curling velocity and the local curvature are mostly determined by the bending stiffness A and practically do not depend on the fiber aspect ratio n, This finding agrees well with the results of another numerical model of LaGrone  $et\ al.\ (2019)$  where only minute changes in the local radius of curvature of the fiber tip and its snaking (analogous to our curling) velocity have been observed in a wide range of relatively large fiber aspect ratios.

#### 6. Universal scaling and phase diagram

#### 6.1. Shapes of fibers with different n and A

The transition from the locally to globally bent fibers, observed for the increasing values of the bending stiffness A and illustrated in figures 10(b,c), motivated us to search for  $\kappa_{b2}n$  as a universal function of  $A/n^{\gamma}$ , with a certain value of the exponent  $\gamma$ . We use here  $\kappa_{b2}n$  because in the global bending mode we expect bending along the whole fiber length. Indeed, in figures 13(a,b), plotted in log-log scale, we find the universal scaling of  $\kappa_{b2}n$ , based on the numerical simulations  $\mathcal{M}_2$  (in a) and  $\mathcal{M}_1$  (in b), respectively. We added to figure 13(a) also the results of the  $\mathcal{M}_2$  simulations reported by Słowicka et al. (2015), with the parameters n = 10,  $L_0/(2a) = 1.01$  and  $k_s = 2000$ . From the numerical data for the model  $\mathcal{M}_2$  we obtain the exponent  $\gamma = 3.25$  and we find the slopes -0.3 and -5 of the two straight lines for the local and global bending regimes, for  $\log_{10}(A/n^{3.25}) \lesssim -2.9$  and  $\log_{10}(A/n^{3.25}) \gtrsim -2.3$ , respectively. The fits agree very well with the results of the  $\mathcal{M}_2$  simulations, and reasonably well with the results of the  $\mathcal{M}_1$  simulations, as shown in figures 13(a) and (b), respectively. The deviations from the universal curve are observed only owing to the excluded volume effects seen for very flexible fibers, with the excluded volume value of the maximum local curvature  $\kappa_{b2} = \log_{10} \sqrt{3} \approx 0.24$ . The deviations correspond to the first (small A) regime of the fiber bending described in section 5.1 and shown in figure 10. For the local bending, the relation  $\log_{10}(\kappa_{b2}n) \sim -0.3\log_{10}(A/n^{3.25}) + 0.48$ , fitted to the  $\mathcal{M}_2$  numerical data, gives the approximate scaling of the maximum curvature  $\kappa_{b2} \sim A^{-0.3}$  independent of n, in agreement with the previous discussion of the local character of the dynamics of very elastic fibers. The exponent -0.3 is close but not identical to -1/4 fitted to the  $\mathcal{M}_1$  numerical data in figure 10(b). In the global bending regime, we find that  $\kappa_{b2}n \sim$  $(A/n^{3.25})^{-5}$ .

The fitting of the exponent  $\gamma$  in the relation  $A/n^{\gamma}$  is based on the choice of 2an to represent the fiber length L, and it is sensitive to a choice of L. For example,  $\gamma \approx 3$  if the fiber length  $L = (n-1)L_0$  is chosen. Such a shorter fiber length was proposed by Farutin et al. (2016) as the result of comparing shapes of flexible fibers and deformable vesicles in Poiseuille flow and partially accounts for the rigidity of the beads at the fiber ends. On the other hand, in shear flow a matching of the tumbling period with the half-period of the Jeffery's orbit could be used to determine L. In the bead model  $\mathcal{M}_2$  for stiffer fibers, the effective aspect ratio L defined in this way is greater than 2an, and it could lead to  $\gamma$  closer to 4, what means also closer to the scaling  $\kappa_{b2} \sim A^{-1/4}$  of the local bending proposed in figure 10(b).

We expect that also the shape of the whole fiber is a universal function of  $A/n^{3.25}$ . Indeed, as illustrated in figure 13, for the models  $\mathcal{M}_2$  (left) and  $\mathcal{M}_1$  (right), the fiber shapes depend on n and A approximately through the ratio  $A/n^{3.25}$ . We show it separately for the global bending in figures 13(c,d) and for the local bending in figures 13(e,f). The corresponding values of  $A/n^{3.25}$  are explicitly indicated below each fiber shape, with approximately the same values for all the similar shapes.

Comparison of the power-law scaling of the fiber shapes with an attempt to find another similarity solution, based on a logarithmic dependence on n and a generalized elastoviscous number, standard in the SBT and elastica approaches, is presented in Appendix C. We show there that, although such a possibility cannot be excluded, it seems to be quite complicated to construct. Using simple arguments, we are able to find such a scaling function only for the local bending mode.

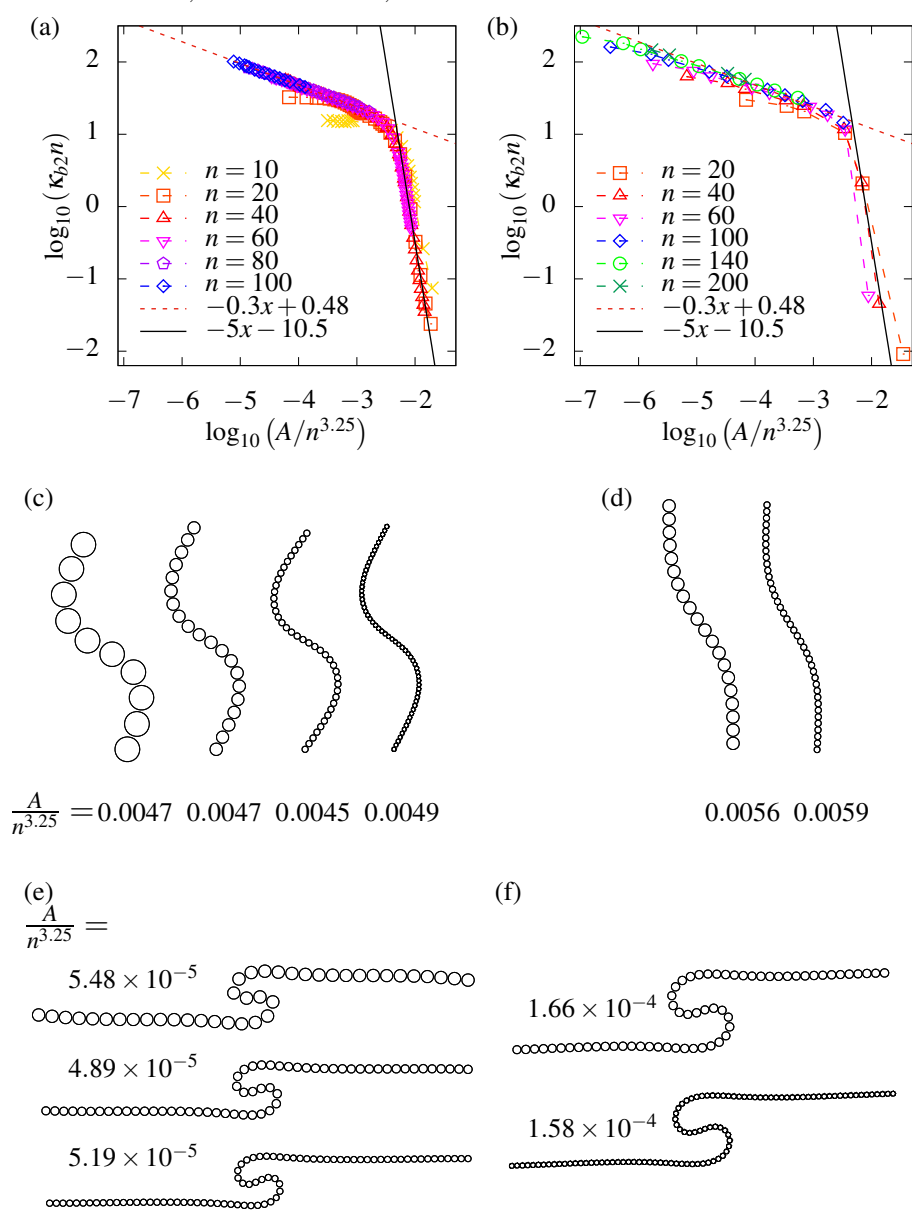


FIGURE 13. Universal similarity scaling of fiber shapes, evaluated with the model  $\mathcal{M}_2$ , (a,c,e) in the left column, and with the model  $\mathcal{M}_1$ , (b,d,f) in the right column. The maximum curvature  $\kappa_{b2}n$ , scaled by the inverse of the fiber length, can be approximated as a universal function of  $A/n^{3.25}$ , as shown in (a-b) in the log-log scale. The regimes of local and global bending correspond to a more flat and a more steep straight lines, respectively. As shown in figures 13(c-f), in both regimes shapes of fibers are almost the same for approximately the same values of  $A/n^{3.25}$  (as indicated). In (c) (n, A) = (10.8.4), (20.79.4), (40.720.6), (60.2922.5), in (d) (n, A) = (20.100), (40.1000), in (e) (n, A) = (40.8.8), (60.29.4), (80.79.4) and in (f) (n, A) = (60.100), (100.500).

#### 6.2. Phase diagram of the dynamical modes

The analysis of the fiber dynamics can be summarized on a phase diagram in the space of the fiber aspect ratio n and the bending stiffness A. In figure 14 we show the

numerical results, with essentially the same features for the bead models  $\mathcal{M}_1$  and  $\mathcal{M}_2$ . The elastic fiber initially aligned with the shear flow has three characteristic modes of motion, depending on values of n and A:

- 1. The fiber does not straighten out again. The curvature  $\kappa$  does not return to zero after the first bend event.
- 2. The fiber bends locally, curls and then stretches; correspondingly curvature grows, reaches a plateau and then returns to zero in a periodic way.
- 3. The fiber periodically bends globally along the whole length. Curvature maxima are observed but the plateau vanishes.

At early times, the fiber is bent only at the ends. During the curling motion, as shown in figures 3 and 12 and earlier by Harasim et al. (2013); Liu et al. (2018); LaGrone et al. (2019), the range of the most curved segments shifts towards the central part of the fiber. The fiber ends become straight and almost aligned with the flow, and the length of straight ends increases with time. Therefore, in general, we might expect that the end of such a long fiber will behave in a similar way as a fiber of a comparable length aligned with the flow. Therefore, if the curling continues long enough, with  $\tau_c \gtrsim \tau_b$ , the fiber may bend its end again, even several times, and it will not straighten out. Indeed, such a scenario sometimes happens for very long or very flexible fibers, as shown in figure 4, and earlier by Nguyen & Fauci (2014); LaGrone et al. (2019). Using our scalings,  $\tau_b \propto A^{1/3}$  and  $\tau_c \propto A^{-1/3} n^{1.17}$ , a dynamical transition could be expected around  $A \propto n^{1.75}$ . However, the physical origin of the transition between the coiled and straightening out modes is more complicated. Shorter fibers cannot bend several times, but still they do not straighten out along the flow when their bending stiffness is small enough.

The transition between the coiled and locally bent modes for shorter fibers with  $n \leq 40$ and a wide range of values of the bending stiffness A has been analyzed by Słowicka et al. (2015). The dynamics of flexible fibers were evaluated over a long time, starting from the initial configuration aligned with the flow. A characteristic value  $A_{CS}(n)$  was found for the transition between the fibers that remain coiled and the fibers that straighten out along the flow while tumbling, with  $A_{CS}(n) \propto n^{3/2}$ . Moreover, the dynamics was shown to be very sensitive to a small change of A close to  $A_{CS}$ . For A slightly below the critical value, fibers often straightened out a smaller or larger number of times before changing to the coiled mode. Słowicka et al. (2015) sorted the data for the modes 1 and 2 based on the long-time behavior. We present in figure 14 (small open symbols) some of the results obtained by Słowicka et al. (2015). The inset illustrates high precision of the critical values  $A_{CS}$  determined there and marked by stars in figure 14. The results of the model  $\mathcal{M}_2$  applied in this work (large open symbols) also support the  $A_{CS}(n) \propto n^{3/2}$ scaling of the transition between the coiled and straightening out modes. The numerical simulations in the  $\mathcal{M}_1$  model also agree well with the above scaling, with a different factor which could be interpreted as the result of different bending potentials in both models.

In contrast to the transition between the modes 1 and 2, the transition between the modes 2 and 3 is not sharp. It takes place in a range of the phase space (n, A) marked gray in figure 14. This stripe corresponds to  $-2.3 \leq \log_{10}(A/n^{3.25}) \lesssim -2.9$ , i.e., the range between the local and global bending found numerically with the bead model  $\mathcal{M}_2$  and shown in figure 13(a), in agreement with the findings of the model  $\mathcal{M}_1$  presented in figure 13(b). The different symbols are the locally and globally bent fibers that indicate just an approximation, based on a comparison of the time instant of the maximum  $\kappa_b$  to the flipping time  $\tau_f$ , as described in Appendix D. In the regime of the local bending, for a smaller A or larger n, the bending time scales as  $\tau_b \propto A^{1/3}$  and the maximum local

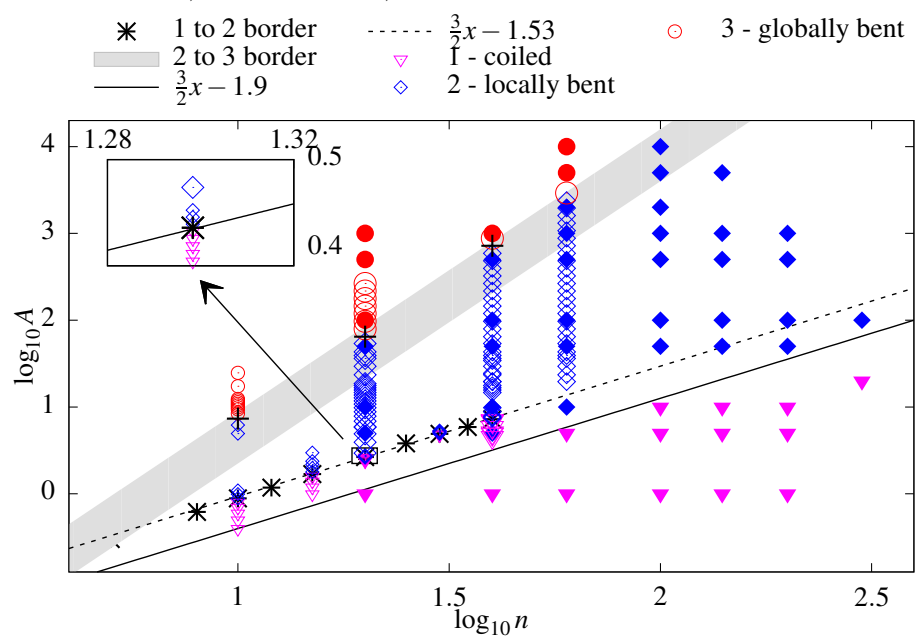


FIGURE 14. Diagram of three dynamical modes in the phase space of the parameters n and A, for the bead models  $\mathcal{M}_1$  (filled symbols) and  $\mathcal{M}_2$  (open symbols). The dynamical modes of the fibers initially aligned with the flow are the following: the fibers that are coiled and do not straighten out (mode 1, triangles); the fibers that straighten out along the flow while tumbling periodically and bend locally (mode 2, rhombus) or globally (mode 3, circles). A sharp transition between the fibers that straighten out while tumbling and the fibers that stay coiled is marked by a dashed line and the stars, taken from (Słowicka et al. 2015), for the  $\mathcal{M}_2$  model and by a solid line for the  $\mathcal{M}_1$  model. In contrast, the transition between fibers bent locally and globally is gradual (gray area). The sizes of symbols for the  $\mathcal{M}_2$  model discriminate between data from this work with  $l_0$ =1.02 and  $k_s$ =1000 (large open symbols) and the data of Słowicka et al. (2015) with  $l_0$ =1.01 and  $k_s$ =2000 (small open symbols).

curvature scales as  $\kappa_b \propto A^{-1/4}$ , independently of n. In the regime of the global bending,  $\tau_b \propto n$  independently of A, and  $\kappa_b n \propto (A/n^{3.25})^{-5}$ .

The transition between the local and global bending could be interpreted as a competition between bending and rotation. If the fiber bends before it manages to rotate in shear flow, it belongs to the local bending mode while if it rotates before it bends, it belongs to the global bending mode. Approximating the rotation time as  $T_J/4 \propto n$ , and equating  $\tau_b \approx T_J/4$ , we obtain  $A \propto n^3$ , which is an approximation of the transition between the local and global bending shown in figure 14. Another way of looking at the transition between the local and global bending is to compare the typical length scales. The length of the bent fiber end at  $\tau_b$  scales as  $A^{1/3}$ . In the local bending mode, it needs to be smaller than half of the fiber length, proportional to n, which again estimates the transition roughly as  $A \propto n^3$ .

#### 7. Conclusions

In this paper, we analyze the evolution of an elastic thin fiber that is initially straight and aligned with an ambient shear flow. We consider a wide range of the fiber aspect ratios n and many different values of the bending stiffness ratio A (i.e., the ratio of the bending forces to the hydrodynamic forces caused by the flow rate  $\dot{\gamma}$ ). We use

two theoretical descriptions of the fiber: the bead-spring model with elastic potential energy and hydrodynamic interactions, and also a generalized elastica model. These two approaches complement each other and allow to rationalize analytically many of the observed numerical results for the bead-spring model.

To quantify evolution of the fiber shapes, we introduce and evaluate numerically three main characteristic time-dependent quantities: the deflection of the fiber tip u(0,t) in the direction perpendicular to the flow, with the first maximum at  $u_{\text{max}}$ , the maximum local curvature  $\kappa(t)$ , with the largest value  $\kappa_{2b} = \max_t \kappa(t)$ , and the curling velocity  $v_x(t)$ , with the maximum value  $v_{xm}$ . Their behavior allows us to identify three characteristic time scales of the dynamics: the bending time  $\tau_b$ , the curling time  $\tau_c$  and the tumbling time  $\tau$  equal to the half-period  $T_J/2$  of the effective Jeffery rotation.

Accordingly to the time scales, we identify three characteristic stages of the time evolution of flexible fibers initially aligned with the flow: bending of the fiber tips for  $0 \le t \le \tau_b$ , curling of the deformation towards the center of the fiber for  $\tau_b \le t \le \tau_b + \tau_c$  and stretching of the fiber for  $\tau_b + \tau_c \le t \le T_J/2$  with an effective Jeffery's period  $T_J$ . In the bending stage, we find the scaling  $u(0,t) \propto (t^3/A)^{1/4}$ , with the maximum  $u_{\text{max}} \propto A^{1/3}$  at  $\tau_b \propto A^{1/3}$ , all independent of n, in agreement with the local character of the early stage of the fiber dynamics for all the modes. In the curling stage, the maximum curvature  $\kappa(t)$  and the curling velocity  $v_x(t)$  are approximately independent of n (except for short final time intervals), and for a sufficiently large n change in time only a little (except for short initial and final time intervals), as argued by Harasim  $et\ al.\ (2013)$  and Liu  $et\ al.\ (2018)$ .

We demonstrate that  $\tau_b/n$ ,  $\kappa_{b2}n$  and  $\tau_c$  depend on n and A approximately through certain universal functions  $A/n^{\alpha}$ . Based on the numerical simulations, we determine the exponents  $\alpha$  which are equal to 3, 3.25 and 3.5, respectively (close to but different than 4 as in case of the elasto-viscous number). In particular, the shapes of fibers (and the maximum 'global' curvature  $\kappa_{h2}n$ ) are shown to depend on n and A approximately through  $A/n^{3.25}$ . Referee suggested to try another similarity function, dependent on log n, for the same reason that slender body theory depends on the logarithm of the aspect ratio. An (unsuccessful) attempt to replace a power law with the exponent 3.25 by a logarithmic dependence is described in Appendix C. In figure 16 we present an analog of figure 13, but with an elasto-viscous number  $\log_{10}[A(\ln n + \ln 2 + 1/2)/n^4]$  on the horizontal axis. The constants in the numerator follow from equation (8.8) for the SBT transverse motion, derived by Batchelor (1970a). Different constants in the logarithmic expressions are also used e.g. by Becker & Shelley (2001) and Young & Shelley (2007). We find it interesting that the plots of  $\kappa_{b2}n$  versus the elasto-viscous number in figure 16 seem to indicate that the fiber shape (at the time of its maximum curvature) might be a universal function of the elasto-viscous number in the local bending mode (left part of the plot) but not in the global bending mode (right part of the plot). The difficulty of matching a logarithmic expression might be related to relatively small values of n in our simulations. A scaling which involves  $\ln n$  might require very large aspect ratios n. It seems logical that comparison of  $\kappa_{b2}n$  for fibers with different thickness and the same length may depend not only on the elasto-viscous number, the parameter adequate for asymptotically large values of n. Moreover, it is known from SBT that the constants added to  $\ln n$  are sensitive to fiber shape. It is also worth remembering that for moderate values of n a constant added to the logarithm has a significant influence. This constant for a flexible, deformed fiber depends on both n and A, and it is difficult to evaluate it theoretically. However, it is clear that its value is different from Batchelor's result for a straight rigid rod. Therefore it is clear that an additive constant for a flexible fiber should depend on shape, and therefore on both n and A.

Based on the numerical simulations, we classify the dynamics of flexible fibers in the phase space of n and A, according to the essential features of the motion and shape deformation. We find three different modes of the fiber motion: coiled, locally bent and globally bent, and we identify the characteristic range of n and A for each of them. The classification refers to the fibers initially aligned with the flow. In the coiled mode, found for larger n or smaller A, the fibers later do not straighten out along the flow, in contrast to the other two modes. Global bending of fibers takes place at smaller n or larger Aand it corresponds to coherent deformation along the whole fiber length. Local bending means that only a part of the fiber is curved, and it is typical for intermediate values of n and A. Essentially, basic features of these three scenarios were identified already in experiments performed by Forgacs & Mason (1959b) who called them a coiled orbit, springy rotation and snake turn, and then analyzed e.g. by Lindström & Uesaka (2007), Harasim et al. (2013), Nguyen & Fauci (2014), Liu et al. (2018) and LaGrone et al. (2019), with differences between shapes observed under different physical conditions (e.g. with or without Brownian motion). Here for the first time a systematic analysis of these three modes is performed.

In particular, all three stages of the evolution are observed for the local bending dynamical mode. In the global bending, the curling stage is absent, and for the coiled mode there is no stretching stage and the curling motion is much more complicated than in case of the local bending mode. For the local bending, we find the approximate scaling  $\kappa_{b2} \propto A^{-0.3}$ † independent of n, with the exponent close to -1/4 found by Harasim et al. (2013) and Liu et al. (2018). The dependence of the global bending on A has not been analyzed. We find that the maximum 'global' curvature  $\kappa_{b2}n \propto (A/n^{3.25})^{-5}$  decays rapidly with A, which is much faster than in the local bending mode.

Our analysis of the dynamics for different n and A indicates that the transition between the local and global bending takes place for  $-2.3 \lesssim \log_{10}(A/n^{3.25}) \lesssim -2.9$ . Therefore, it is close but not exactly equal to a certain universal value of the elasto-viscous number  $\bar{\eta} = \frac{8\pi\mu_0\dot{\gamma}(2a)^4n^4}{EI\ln(\epsilon^{-1})}$ ‡, which scales as  $n^4/A$  (Becker & Shelley 2001; Tornberg & Shelley 2004; Harasim et al. 2013; Nguyen & Fauci 2014; Liu et al. 2018; LaGrone et al. 2019). Moreover, we have found that a second transition, between the coiled fibers and the fibers that straighten out, is given as  $\log_{10}(A/n^{3/2}) = C$  and it takes place at different values of the elasto-viscous number when n or A are changed. Therefore, we find it beneficial to extend the concept of the elasto-viscous number and analyze the dynamics in the phase-space of n and A. Certain features of the dynamics depend on n and A in a more complex way than the elasto-viscous number predicts.

We also analyze the elastica model and rationalize some of the scalings described above. We provide a self-similar exact solution of the linear elastica equations when the fiber is almost aligned with the flow. The main new idea is to assume as the boundary condition the existence of a constant hydrodynamic force exerted on the fiber tip by the rate-of-strain of the ambient flow. This allows tracing the early stage of the fiber bending from the initial position aligned with the flow which, is not possible within the standard elastica approach. Moreover, we derive such a hydrodynamic force from the theory of hydrodynamic interactions and evaluate it numerically. These findings indicate that the standard elastica model in some cases may be too simple to predict the dynamics, and cannot always serve as a source of a theoretical explanation.

<sup>†</sup> In the  $\mathcal{M}_1$  model we can also deduce from the numerical results that  $\kappa_{b2} \propto A^{-1/4}$ , see figure 9(b). In this case, our data seem to agree with both scalings.

 $<sup>\</sup>ddagger$  or effective viscosity (effective flow forcing)  $\bar{\mu}=\frac{8\pi\mu_0\dot{\gamma}(2a)^4n^4}{EI}$ 

#### Acknowledgements

We thank Basile Audoly for helpful discussion. We are grateful to the referees for useful remarks. We benefited from the ITHACA project PPI/APM/2018/1/00045 financed by the Polish National Agency for Academic Exchange. P.J.Z. and M.E.J. were supported in part by the Polish National Science Centre under grant UMO-2018/31/B/ST8/03640. H.A.S. acknowledges support from NSF grant CMMI-1661672.

# A. Hydrodynamic interactions in GRPY and Hydromultipole models

The GRPY approximation generalizes the Rotne-Prager (Rotne & Prager 1969; Yamakawa 1970) and Goldstein (Goldstein 1985) analytical expressions for the translational and rotational mobilities to the dipolar degrees of freedom, for both non-overlapping and overlapping spherical particles of different radii (Wajnryb et al. 2013; Zuk et al. 2014, 2017). The GRPY includes pairwise hydrodynamic interactions through the analytic positive-definite mobility matrices acting on the lowest force multipoles induced at the sphere surfaces by the fluid flow (Kim & Karrila 1991). In this way, the GRPY approximation takes some of the ideas from the method of reflections (Kim & Karrila 1991), Stokesian dynamics developed by Durlofsky et al. (1987) and Brady & Bossis (1988) and the multipole expansion performed by Felderhof (1988) and Cichocki et al. (1994, 1999). Although the GRPY does not include the lubrication interactions, by construction it gives positive definite mobility matrices for overlapping spheres which can be easily used for soft objects allowing for overlaps of the particle surfaces.

In this work, mobility matrix was used for the Lees-Edwards (Lees & Edwards 1972) periodic boundary conditions with the Generalized Rotne-Prager-Yamakawa model of hydrodynamic interactions derived by Mizerski et al. (2014). The periodic box was elongated in the direction of the shear flow so has dimensions  $L_x, L_y, L_z$ , with ratio  $L_x: L_y: L_z=4:1:1$ . The volume of the computational cell was set for each fiber length separately and we kept the volume fraction occupied by the fiber smaller then  $10^{-5}$  to have  $L_x, L_y, L_z \gg 2na$ . For such a large periodic cell the values of the hydrodynamic tensors differ from the values of the hydrodynamic tensors in the case without periodic boundary conditions on the level of the numerical accuracy when using double precision calculations.

#### A.2. Hydromultipole - model 2

Consider now a general system of n spherical particles immersed in an incompressible fluid flow with velocity  $\mathbf{V}(\mathbf{R})$  and pressure  $p(\mathbf{R})$  that satisfies the quasi-steady Stokes equations with the boundary condition at infinity,

$$\mathbf{V}(\mathbf{R}) - \mathbf{V}_{\infty}(\mathbf{R}) \to 0$$
, when  $R \to \infty$ , (A.1)

where  $V_{\infty}(\mathbf{R})$  is an arbitrary external fluid flow. Assume the no-slip boundary conditions at the bead surfaces,  $S_i$ ,

$$\mathbf{V}(\mathbf{R}) = \mathbf{W}_i(\mathbf{R}) \equiv \mathbf{U}_i + \mathbf{\Omega}_i \times (\mathbf{R} - \mathbf{R}_i), \text{ for } \mathbf{R} \in S_i, \quad i = 1, ..., n.$$
(A.2)

The integral representation (Pozrikidis 1992) and the method of induced forces (Cox & Brenner 1967; Mazur & Bedeaux 1974; Felderhof 1976) can be used to express the fluid velocity in terms of the Oseen tensor  $\mathbf{T}_0(\mathbf{R} - \bar{\mathbf{R}})$ , given e.g. by (Kim & Karrila 1991), applied to the density  $\mathbf{f}_j(\mathbf{R})$  of the forces exerted by the surface of the particle i on the fluid. Application of the boundary conditions (A.2) results in the boundary integral

equation for the force density  $\mathbf{f}_i(\mathbf{R})$ ,

$$\mathbf{W}_i(\mathbf{R}) - \mathbf{V}_{\infty}(\mathbf{R}) = \sum_{j=1}^n \int \mathbf{T}_0(\mathbf{R} - \bar{\mathbf{R}}) \cdot \mathbf{f}_j(\bar{\mathbf{R}}) d\bar{\mathbf{R}}, \quad \mathbf{R} \in S_i \text{ and } \bar{\mathbf{R}} \in S_j,$$
 (A.3)

which is then projected onto a complete set of elementary (spherical multipole) solutions of the Stokes equations (Felderhof 1988; Cichocki et al. 1988). As a result, an infinite set of algebraic equations is obtained. This set is truncated at a certain multipole order L and solved for the vector of the force multipoles. Converting from the spherical to the Cartesian representation, we obtain a linear relation between 1) the forces  $F_i$ , torques  $T_i$ , stresslets  $S_i$  and higher-order force multipoles exerted on the fluid by the particles i = 1, ..., N, and 2) the translational and rotational velocities,  $U_j$  and  $\Omega_j$  of particle j = 1, ..., N, and the multipoles of the external velocity field  $V_{\infty}(\mathbf{R})$ . This relation is written using the grand friction matrix  $\zeta$ ,

$$\begin{pmatrix} \tilde{F} \\ \tilde{T} \\ \tilde{S} \\ \dots \end{pmatrix} = - \begin{pmatrix} \zeta^{tt} & \zeta^{tr} & \zeta^{td} & \dots \\ \zeta^{rt} & \zeta^{rr} & \zeta^{rd} & \dots \\ \zeta^{dt} & \zeta^{dr} & \zeta^{dd} & \dots \\ \dots & \dots & \dots & \dots \end{pmatrix} \cdot \begin{pmatrix} \tilde{V}_{\infty} - \tilde{U} \\ \tilde{\omega}_{\infty} - \tilde{\Omega} \\ \tilde{E}_{\infty} \\ \dots \end{pmatrix}. \tag{A.4}$$

In the above the 3N dimensional vectors are  $\tilde{F} = (F_1, F_2, \dots, F_N)$ ,  $\tilde{T} = (T_1, T_2, \dots, T_N)$ ,  $\tilde{U} = (U_1, U_2, \dots, U_N)$ ,  $\tilde{Q} = (\Omega_1, \Omega_2, \dots, \Omega_N)$ . The velocity multipoles are evaluated at the centers  $\mathbf{R}_i$  of the particle  $i = 1, \dots, N$  from the external flow velocity and its derivatives. In particular,  $\tilde{V}_{\infty} = (\mathbf{V}_{\infty}(\mathbf{R}_1), \dots, \mathbf{V}_{\infty}(\mathbf{R}_N))$ . Similarly  $\tilde{\omega}_{\infty}$  is the vector of vorticities, with  $\omega_{\infty}(\mathbf{R}_i) = \frac{1}{2}(\nabla \times \mathbf{V}_{\infty})|_{\mathbf{R}_i}$ . Next we introduce the tensor of strain rates  $\tilde{E}_{\infty} = (\mathbf{E}_{\infty}(\mathbf{R}_1), \dots, \mathbf{E}_{\infty}(\mathbf{R}_N))$  with  $E_{\infty}(\mathbf{R}_i) = \frac{1}{2}(\nabla \mathbf{V}_{\infty} + (\nabla \mathbf{V}_{\infty})^T)|_{\mathbf{R}_i}$ . The second rank strain tensors  $E_{\infty}(\mathbf{R}_i)$  are symmetric and traceless and therefore  $\tilde{E}_{\infty}$  has 5N independent components. Finally, the symmetric tensor  $\tilde{S} = (\mathbf{S}_1, \dots, \mathbf{S}_N)$  represents the particle stresslets. To speed up the convergence of the multipole expansion, the lubrication correction is applied to friction matrices, as described by Durlofsky *et al.* (1987), Sangani & Mo (1994) and Cichocki *et al.* (1999).

The system of the particles evolves according to velocities calculated with the use of the grand mobility matrix  $\mu$ 

$$\begin{pmatrix}
\tilde{U} - \tilde{V}_{\infty} \\
\tilde{\Omega} - \tilde{\omega}_{\infty} \\
-\tilde{\mathcal{S}}
\end{pmatrix} = \begin{pmatrix}
\mu^{tt} & \mu^{tr} & \mu^{td} & \dots \\
\mu^{rt} & \mu^{rr} & \mu^{td} & \dots \\
\mu^{dt} & \mu^{dr} & \mu^{dd} & \dots \\
\dots & \dots & \dots & \dots
\end{pmatrix} \cdot \begin{pmatrix}
\tilde{F} \\
\tilde{T} \\
\tilde{E}_{\infty} \\
\dots
\end{pmatrix}$$
(A.5)

which is a partial inversion of the relation (A.4), i.e., note that  $\tilde{\mathbf{S}}$  is now grouped with generalized velocities and  $\tilde{\mathbf{E}}_{\infty}$  with generalized forces. The superscripts t, r and d denote translational, rotational and dipolar degrees of freedom of the grand friction and grand mobility matrices  $\boldsymbol{\zeta}$  and  $\boldsymbol{\mu}$ , respectively. The hydrodynamic matrices  $\boldsymbol{\zeta}$  and  $\boldsymbol{\mu}$  in general depend on the positions of all the particles in the system. In particular, for the external shear flow and in the absence of external torques, equation (A.5) leads to equation (2.7) for the translational velocities of the fiber beads that make up the fiber.

# B. Comparing results from the $\mathcal{M}_1$ and $\mathcal{M}_2$ models

In this Appendix, we compare in detail the results for the curvature  $\kappa_{b2}$  obtained with the use of the  $\mathcal{M}_1$  and  $\mathcal{M}_2$  bead models and discuss the physical reason for the small

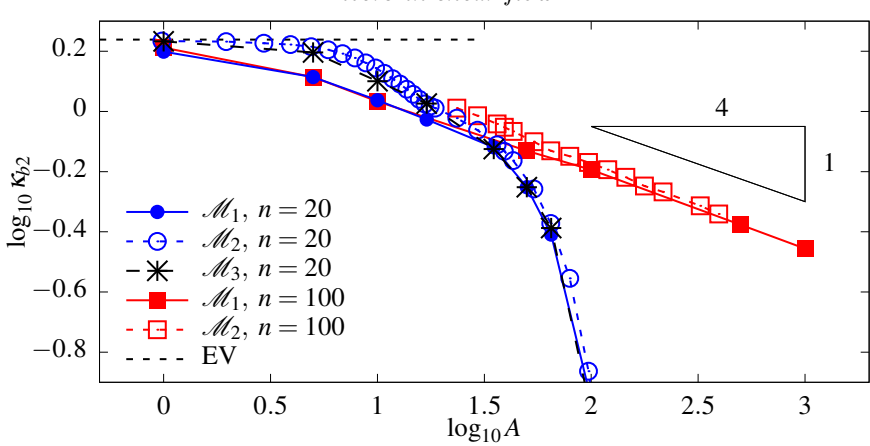


FIGURE 15. Comparison of three bead models of a flexible fiber. The maximum curvature  $\kappa_{b2}$  vs. bending stiffness A, evaluated with the use of the models  $\mathcal{M}_1$  (filled symbols),  $\mathcal{M}_2$  (empty symbols) and  $\mathcal{M}_3$  (stars). The excluded volume (EV) limit is marked as the horizontal dashed line.

differences. We start from a brief reminder of both models, described in Sec. 2.1. Hydrodynamic interactions in the bead model  $\mathcal{M}_1$  are approximated using the generalized Rotne-Prager-Yamakawa mobility matrices. The treatment of the hydrodynamic interactions in the bead model  $\mathcal{M}_2$  is based on the multipole expansion corrected for lubrication, as described in Appendices 2.1.2, A.2 and implemented in the precise numerical codes Hydromultipole. The repulsive part of the Lennard-Jones potential energy (2.6) used in  $\mathcal{M}_1$  is not needed (and therefore not present) in the model  $\mathcal{M}_2$ , because of the stick boundary conditions at the bead surfaces and the lubrication hydrodynamic forces that are taken into account.

In the  $\mathcal{M}_1$  approach, the elastic properties are determined by the sum of the FENE (finitely extensible nonlinear elastic) stretching and harmonic bending potential energies defined in equations (2.2) and (2.3), respectively. In the  $\mathcal{M}_2$  approach, the elastic properties are determined by the sum of the Hookean stretching and cosine (Kratky-Porod) bending potential energies defined in equations (2.4) and (2.5), respectively. The elastic constitutive laws (set 1 or set 2, see table 1) in the models  $\mathcal{M}_1$  and  $\mathcal{M}_2$  are the same for small deformations, but have different forms for a significant change of the fiber length (which is irrelevant because the fiber practically does not extend) and for large bending angles (which is important because we consider highly bent fibers).

It is known from Bukowicki & Ekiel-Jeżewska (2018) that different bending potential energies can result in significant differences of the dynamics of flexible fibers in case of large bending angles, which correspond to a large curvature. Therefore we investigate if this effect is responsible for the differences between the dependence of  $\kappa_b$  on A resulting from the models  $\mathcal{M}_1$  and  $\mathcal{M}_2$  and shown in figures 10(b,c). To this goal we introduce a third bead model  $\mathcal{M}_3$  and apply it in test simulations. In the  $\mathcal{M}_3$  model, hydrodynamic interactions are treated with the GRPY approach supplemented with equation. (2.6) as in  $\mathcal{M}_1$ , but the elastic constitutive laws are given by equations (2.4), (2.5) as in  $\mathcal{M}_2$ . The difference between the stretching potential energies is irrelevant because the fiber length practically does not change. The essential difference between  $\mathcal{M}_1$  and  $\mathcal{M}_3$  is the the difference between harmonic and cosine bending potential energies.

Figure 15 presents comparison of the behavior of the three fiber models for n=20 and n=100 elucidating the differences between the models. For n=20, the maximum curvature  $\kappa_{b2}$  is evaluated with the models  $\mathcal{M}_1$ ,  $\mathcal{M}_2$ ,  $\mathcal{M}_3$  and plotted in the log-log scale

in figure 15. For  $A \lesssim 20-30$  there is a difference between  $\mathcal{M}_1$  and  $\mathcal{M}_2$ , and also between  $\mathcal{M}_1$  and  $\mathcal{M}_3$ . However, the results from  $\mathcal{M}_2$ ,  $\mathcal{M}_3$  are close to each other. Therefore the form of the bending potential at large angles seems to be essential for the dynamics of more flexible fibers, in agreement with the same conclusion for sedimenting flexible fibers given in Bukowicki & Ekiel-Jeżewska (2018).

Indeed the cosine bending potential from the models  $\mathcal{M}_2$  and  $\mathcal{M}_3$  is more flexible than harmonic bending potential from  $\mathcal{M}_1$  and for large bends it leads to higher curvatures. For such large values of the bending stiffness that the radius of curvature is three or more times larger than the bead radius, the maximum curvatures obtained with the models  $\mathcal{M}_1$ ,  $\mathcal{M}_2$ ,  $\mathcal{M}_3$  are the same because the bending potential energies behave alike.† This is expected since both are intended to approximate the elastic bending potential energy in the limit of large A.

The agreement between the  $\mathcal{M}_1$ ,  $\mathcal{M}_2$  and  $\mathcal{M}_3$  models of more stiff fibers is illustrated in figure 15 where we also present the maximum curvature  $\kappa_{b2}$  for much longer fibers with n = 100, evaluated with  $\mathcal{M}_1$  and  $\mathcal{M}_2$  models. For  $A \gtrsim 100$  a good agreement is obtained between all the computations performed with the use of  $\mathcal{M}_1$  and  $\mathcal{M}_2$  models, regardless of the fiber length. Actually, all the properties of flexible fibers that were discussed in the main text for the model  $\mathcal{M}_1$  are analogous for the model  $\mathcal{M}_2$  in the range of intermediate and large A, where the constitutive laws are manifesting similar behavior.

## C. Discussion of the universal scaling

The idea of figures 13(c-f) and 16(b-c) is to compare properties of fibers of the same length, but different thickness and different bending stiffness. To this goal, on vertical axis we plotted the maximum curvature normalized by the inverse fiber length (rather than by its inverse width), i.e.,  $\kappa_{b2}n$ . The universal scaling of the maximum curvature  $\kappa_{b2}n$ , provided in §6.1, is based on the similarity solution as a function of  $A/n^{3.25}$ . Here we check if a universal scaling can be based on a certain modification of the standard elasto-viscous number, including a logarithmic dependence on n. Therefore in 16(a) we plot in log-log scale  $\kappa_{b2}n$  versus the elasto-viscous number  $A(\ln n + \ln 2 + 1/2)/n^4$ , with the constant modified following SBT of Batchelor (1970a). The scaling works reasonably well for the local bending mode, as shown in figure 16(b), but does not account for the global bending mode, as shown in figure 16(c). Possible reasons for this discrepancy are discussed in section 7.

<sup>†</sup> It was estimated by (Bukowicki & Ekiel-Jeżewska 2018) that a difference smaller than 5% is expected for the maximum bending angles  $\pi - \theta_i = \kappa \lesssim 0.7$ .

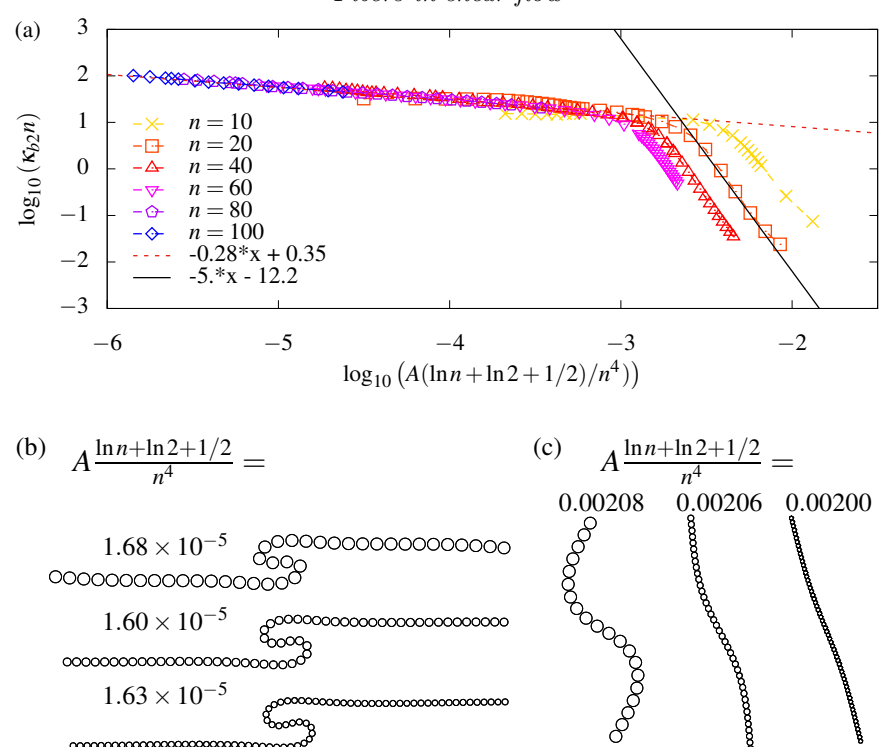


FIGURE 16. The elasto-viscous number  $A(\ln n + \ln 2 + 1/2)/n^4$ , based on the SBT by Batchelor (1970a), is not a universal scaling function of the numerical results obtained with the model  $\mathcal{M}_2$ . (a) The maximum curvature  $\kappa_{b2}n$ , scaled by the inverse of the fiber length, is plotted in the log-log scale versus the elasto-viscous number  $A(\ln n + \ln 2 + 1/2)/n^4$ . The similarity scaling of shapes is observed in (b) for the local bending mode, but it does not work in (c) for the global bending, with values of the elasto-viscous number as indicated. In (b) (n, A) = (40, 8.8), (60, 39.2), (80, 119.6) and in (c) (n, A) = (20, 79.4), (40, 1078.4), (60, 4902.0), respectively.

# D. Time scales close to the transition between local and global bending

In Sec. 6, the distinction between the locally and globally bent fibers was approximately estimated by comparing the time instant of the maximum  $\kappa_b$  with the flipping time (Słowicka et al. 2015, 2020; Farutin et al. 2016), i.e., the time when two end beads have the same x coordinate. This procedure is illustrated in figure 17 using the numerical data from the model  $\mathcal{M}_2$ . If flipping occurs before maximum of  $\kappa_b$ , the corresponding point (n, A) is marked by a square in the phase diagram (figure 14), while if flipping happens at or after  $\kappa_b$  – by a plus or a circle, respectively. However, it should be kept in mind that the change between the locally and globally bent fibers takes place in a certain range of A. The values marked by the symbols + in figure 14 correspond already to the global mode scaling  $\kappa_{b2}n \propto (A/n^{3.25})^{-5}$  but they are too large to satisfy  $\kappa_{b2} \propto A^{-1/4}$  typical for the local bending. The shapes at the maximum curvature shown in figures 17(b-c) are bent globally, but the shape presented in figure 17(a) is not locally bent. In the local bending mode, at the moment of the maximum local curvature, the fiber ends are almost parallel to the flow.

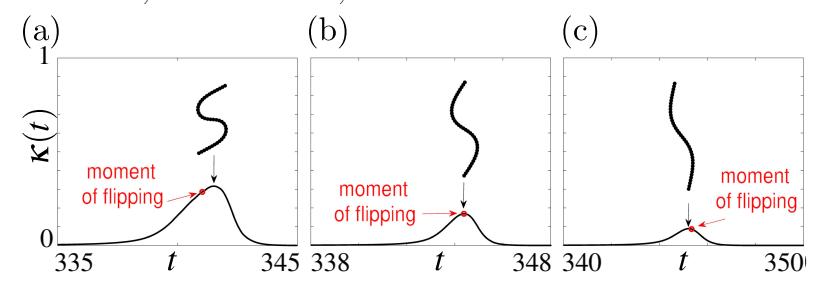


FIGURE 17. Characteristic fiber shapes at the time of the maximum curvature, shown for n=40 and (a) A=483.3, (b) A=720.6, (c) A=880.4. For the global bending mode, the maximum of the local curvature is observed at the flipping moment or later, as in (b) and (c).

#### REFERENCES

AUDOLY, B. 2015 Introduction to the elasticity of rods. In *Fluid-Structure Interactions in Low-Reynolds-Number Flows* (ed. C. Duprat & H. A. Stone), pp. 1–24. Royal Society of Chemistry.

Audoly, B. & Pomeau, Y. 2000 Elasticity and geometry. In Peyresq Lectures On Nonlinear Phenomena, pp. 1–35. World Scientific.

BARENBLATT, G. I. 1996 Scaling, self-similarity, and intermediate asymptotics. Cambridge Texts in Applied Mathematics. Cambridge University Press.

Batchelor, GK 1970a Slender-body theory for particles of arbitrary cross-section in Stokes flow. Journal of Fluid Mechanics 44 (3), 419–440.

Batchelor, G. K. 1970b The stress system in a suspension of force-free particles. J. Fluid Mech. 41 (3), 545–570.

Becker, L. E. & Shelley, M. J. 2001 Instability of elastic filaments in shear flow yields first-normal-stress differences. *Phys. Rev. Lett.* 87 (19), 198301.

Brady, J. F. & Bossis, G. 1988 Stokesian dynamics. Ann. Rev. Fluid Mech. 20, 111–157.

Bretherton, F. P. 1962 The motion of rigid particles in a shear flow at low Reynolds number. Journal of Fluid Mechanics 14 (2), 284–304.

Bukowicki, M. & Ekiel-Jeżewska, M. L. 2018 Different bending models predict different dynamics of sedimenting elastic trumbbells. *Soft Matter* **14** (28), 5786–5799.

Chakrabarti, B., Liu, Y., Lagrone, J., Cortez, R., Fauci, L., du Roure, O., Saintillan, D. & Lindner, A. 2020 Flexible filaments buckle into helicoidal shapes in strong compressional flows. *Nat. Phys.* pp. 1–6.

CICHOCKI, B., EKIEL-JEZEWSKA, M.L. & WAJNRYB, E. 2012 Intrinsic viscosity for Brownian particles of arbitrary shape. *J. Phys.: Conf. Ser.* **392**, 012004.

CICHOCKI, B., EKIEL-JEŻEWSKA, M. L. & WAJNRYB, E. 1999 Lubrication corrections for three-particle contribution to short-time self-diffusion coefficients in colloidal dispersions. J. Chem. Phys. 111 (7), 3265–3273.

CICHOCKI, B., FELDERHOF, B. U., HINSEN, K., WAJNRYB, E. & BŁAWZDZIEWICZ, J. 1994 Friction and mobility of many spheres in Stokes flow. *J. Chem. Phys.* **100**, 3780–3790.

CICHOCKI, B., FELDERHOF, B. U. & SCHMITZ, R. 1988 Hydrodynamic interactions between two spherical particles. *Physicochem. Hydrodyn.* **10**, 383–403.

CORTEZ, R., FAUCI, L. & MEDOVIKOV, A. 2005 The method of regularized Stokeslets in three dimensions: analysis, validation, and application to helical swimming. *Phys. Fluids* **17** (3), 031504.

Cox, R. G. 1970 The motion of long slender bodies in a viscous fluid Part 1. General theory. J. Fluid Mech. 44 (4), 791–810.

Cox, R. G. & Brenner, H. 1967 Effect of finite boundaries on the Stokes resistance of an arbitrary particle Part 3. Translation and rotation. *J. Fluid Mech.* **28** (2), 391–411.

DHONT, J.K.G. & BRIELS, W.J. 2007 Rod-like Brownian particles in shear flow. In *Complex Colloidal Suspensions* (ed. G. Gompper & M. Schick), *Soft Matter*, vol. 2, pp. 216–283. Wiley-VCH Verlag.

DUPRAT, C. & STONE, H. A. 2015 Model problems coupling elastic boundaries and viscous

- flows. In Fluid-Structure Interactions in Low-Reynolds-Number Flows (ed. C. Duprat & H. A. Stone), pp. 78–99. Royal Society of Chemistry.
- Durlofsky, L., Brady, J. F. & Bossis, G. 1987 Dynamic simulation of hydrodynamically interacting particles. *J. Fluid Mech.* **180**, 21–49.
- EGGERS, J. & FONTELOS, M. A. 2015 Singularities: formation, structure, and propagation, Cambridge Texts in Applied Mathematics, vol. 53. Cambridge University Press.
- EKIEL-JEŻEWSKA, M. L. & WAJNRYB, E. 2009 Precise multipole method for calculating hydrodynamic interactions between spherical particles in the Stokes flow. In *In Theoretical Methods for Micro Scale Viscous Flows* (ed. F. Feuillebois & A. Sellier), pp. 127–172. Transworld Research Network, Kerala.
- FARUTIN, A., PIASECKI, T., SŁOWICKA, A. M., MISBAH, C., WAJNRYB, E. & EKIEL-JEŻEWSKA, M. L. 2016 Dynamics of flexible fibers and vesicles in Poiseuille flow at low Reynolds number. Soft Matter 12 (35), 7307–7323.
- FELDERHOF, B. U. 1976 Force density induced on a sphere in linear hydrodynamics: II. Moving sphere, mixed boundary conditions. *Physica A* 84 (3), 569–576.
- Felderhof, B. U. 1988 Many-body hydrodynamic interactions in suspensions. *Physica A* 151, 1-16.
- FÉREC, J., AUSIAS, G., HEUZEY, M. C. & CARREAU, P. J. 2009 Modeling fiber interactions in semiconcentrated fiber suspensions. *J. Rheol.* **53** (1), 49–72.
- FORGACS, O. L. & MASON, S. G. 1959a Particle motions in sheared suspensions IX. Spin and deformation of threadlike particles. J. Coll. Sci. Imp. U. Tok. 14 (5), 457–472.
- Forgacs, O. L. & Mason, S. G. 1959b Particle motions in sheared suspensions: X. Orbits of flexible threadlike particles. J. Coll. Sci. Imp. U. Tok. 14 (5), 473–491.
- GAUGER, E. & STARK, H. 2006 Numerical study of a microscopic artificial swimmer. *Phys. Rev.* E 74 (2), 021907.
- Goldstein, R. F. 1985 Macromolecular diffusion constants: a calculational strategy. *J. Chem. Phys.* 83 (5), 2390–2397.
- Graham, M. D. 2018 Microhydrodynamics, Brownian motion, and complex fluids, , vol. 58. Cambridge University Press.
- HARASIM, M., WUNDERLICH, B., PELEG, O., KRÖGER, M. & BAUSCH, A. R. 2013 Direct observation of the dynamics of semiflexible polymers in shear flow. *Phys. Rev. Lett.* 110 (10), 108302.
- HARDING, S.E. 1997 The intrinsic viscosity of biological macromolecules. Prog. Biophys. Mol. Biol. 68, 207–262.
- HINCH, E. J. 1976 The distortion of a flexible inextensible thread in a shearing flow. J. Fluid Mech.  $\bf 74$  (2), 317-333.
- HINCH, E. J. & LEAL, L. G. 1979 Rotation of small non-axisymmetric particles in a simple shear flow. *J. Fluid Mech.* **92** (3), 591–607.
- JEFFERY, G. B. 1922 The motion of ellipsoidal particles immersed in a viscous fluid. P. R. Soc. Lond. A-Conta. 102 (715), 161–179.
- Jendrejack, R. M., Schwartz, D. C., de Pablo, J. J. & Graham, M. D. 2004 Shear-induced migration in flowing polymer solutions: Simulation of long-chain DNA in microchannels. *J. Chem. Phys.* **120** (5), 2513–2529.
- JOHNSON, R. E. 1980 An improved slender-body theory for Stokes flow. J. Fluid Mech. 99 (2), 411–431.
- JOUNG, C. G., PHAN-THIEN, N. & FAN, X. J. 2001 Direct simulation of flexible fibers. J. Non-Newton. Fluid 99 (1), 1–36.
- Kantsler, V. & Goldstein, R. E. 2012 Fluctuations, dynamics, and the stretch-coil transition of single actin filaments in extensional flows. *Phys. Rev. Lett.* **108** (3), 038103.
- Keller, J. B. & Rubinow, S. I. 1976 Slender-body theory for slow viscous flow. J. Fluid Mech. 75 (4), 705–714.
- Khare, R., Graham, M. D. & de Pablo, J. J. 2006 Cross-stream migration of flexible molecules in a nanochannel. *Phys. Rev. Lett.* **96** (22), 224505.
- Kim, S. & Karrila, S.J 1991 Microhydrodynamics: principles and selected applications. Butterworth-Heinemann.
- Kuei, S., Słowicka, A. M., Ekiel-Jeżewska, M. L., Wajnryb, E. & Stone, H. A. 2015

- Dynamics and topology of a flexible chain: knots in steady shear flow. New J. Phys. 17 (5), 053009.
- LAGRONE, J., CORTEZ, R., YAN, W. & FAUCI, L. 2019 Complex dynamics of long, flexible fibers in shear. J. Non-Newton. Fluid 269, 73–81.
- LARSON, R. G., Hu, H., SMITH, D. E. & CHU, S. 1999 Brownian dynamics simulations of a DNA molecule in an extensional flow field. *J. Rheol.* **43** (2), 267–304.
- LEDUC, P., HABER, C., BAO, G. & WIRTZ, D. 1999 Dynamics of individual flexible polymers in a shear flow. *Nature* **399** (6736), 564–566.
- Lees, A. W. & Edwards, S. F. 1972 The computer study of transport processes under extreme conditions. J. Phys. C 5 (15), 1921.
- LINDNER, A. & SHELLEY, M. J. 2015 Elastic fibers in flows. In *Fluid-Structure Interactions in Low Reynolds Number Flows* (ed. C. Duprat & H. A. Stone), pp. 168–189. Royal Society of Chemistry.
- LINDSTRÖM, S. B. & UESAKA, T. 2007 Simulation of the motion of flexible fibers in viscous fluid flow. *Phys. Fluids* **19** (11), 113307.
- LIU, Y., CHAKRABARTI, B., SAINTILLAN, D., LINDNER, A. & DU ROURE, O. 2018 Morphological transitions of elastic filaments in shear flow. *P. Natl. Acad. Sci. US* 115 (38), 9438–9443.
- MA, H. & GRAHAM, M. D. 2005 Theory of shear-induced migration in dilute polymer solutions near solid boundaries. *Phys. Fluids* **17** (8), 083103.
- MATTHEWS, R., LOUIS, A. A. & YEOMANS, J. M. 2010 Complex dynamics of knotted filaments in shear flow. *Europhys. Lett.* **92** (3), 34003.
- MAZUR, P. & BEDEAUX, D. 1974 A generalization of faxén's theorem to nonsteady motion of a sphere through an incompressible fluid in arbitrary flow. *Physica* **76** (2), 235–246.
- MIZERSKI, K. A., WAJNRYB, E., ZUK, P. J. & SZYMCZAK, P. 2014 The Rotne-Prager-Yamakawa approximation for periodic systems in a shear flow. *J. Chem. Phys.* **140** (18), 184103.
- NARSIMHAN, V., KLOTZ, A. R. & DOYLE, P. S. 2017 Steady-state and transient behavior of knotted chains in extensional fields. ACS Macro Lett. 6 (11), 1285–1289.
- NAZOCKDAST, E. N., RAHIMIAN, A., ZORIN, D. & SHELLEY, M. J. 2017 A fast platform for simulating semi-flexible fiber suspensions applied to cell mechanics. *J. Comput. Phys.* **329**, 173–209.
- NGUYEN, H. & FAUCI, L. 2014 Hydrodynamics of diatom chains and semiflexible fibres. J. R. Soc. Interface 11 (96), 20140314.
- OSEEN, C. W. 1927 Neuere methoden und ergebnisse in der hydrodynamik. Akademische Verlagsgesellschaft.
- Peskin, C. S. 2002 The immersed boundary method. Acta Numer. 11, 479–517.
- Pozrikidis, C. 1992 Boundary integral and singularity methods for linearized viscous flow. Cambridge University Press.
- ROTNE, J. & PRAGER, S. 1969 Variational treatment of hydrodynamic interaction in polymers. J. Chem. Phys. **50**, 4831–4837.
- Du Roure, O., Lindner, A., Nazockdast, E. N. & Shelley, M. J. 2019 Dynamics of flexible fibers in viscous flows and fluids. *Ann. Rev. Fluid Mech.* **51**, 539–572.
- SANGANI, A. S. & Mo, G. 1994 Inclusion of lubrication forces in dynamic simulations. *Phys. Fluids* **6** (5), 1653–1662.
- Schmid, C. F. & Klingenberg, D. J. 2000 Mechanical flocculation in flowing fiber suspensions. *Phys. Rev. Lett.* **84** (2), 290.
- Skjetne, P., Ross, R. F. & Klingenberg, D. J. 1997 Simulation of single fiber dynamics. *J. Chem. Phys.*  $\bf 107$  (6), 2108–2121.
- Słowicka, A. M., Ekiel-Jeżewska, M. L., Sadlej, K. & Wajnryb, E. 2012 Dynamics of fibers in a wide microchannel. J. Chem. Phys. 136 (4), 044904.
- SŁOWICKA, A. M., STONE, H. A. & EKIEL-JEŻEWSKA, M. L. 2020 Flexible fibers in shear flow approach attracting periodic solutions. *Phys. Rev. E* **101** (2), 023104.
- SŁOWICKA, A. M., WAJNRYB, E. & EKIEL-JEŻEWSKA, M. L. 2013 Lateral migration of flexible fibers in Poiseuille flow between two parallel planar solid walls. *Eur. Phys. J. E* **36** (3), 31.

- SLOWICKA, A. M., WAJNRYB, E. & EKIEL-JEŻEWSKA, M. L. 2015 Dynamics of flexible fibers in shear flow. J. Chem. Phys. 143 (12), 124904.
- SMITH, D. E., BABCOCK, H. P. & CHU, S. 1999 Single-polymer dynamics in steady shear flow. Science 283 (5408), 1724–1727.
- Soh, B. W., Klotz, A. R. & Doyle, P. S. 2018 Untying of complex knots on stretched polymers in elongational fields. *Macromolecules* **51** (23), 9562–9571.
- SWITZER III, L. H. & KLINGENBERG, D. J. 2003 Rheology of sheared flexible fiber suspensions via fiber-level simulations. *J. Rheol.* 47 (3), 759–778.
- THORP, I. R. & LISTER, J. R. 2019 Motion of a non-axisymmetric particle in viscous shear flow. J. Fluid Mech. 872, 532–559.
- TORNBERG, A.-K. & SHELLEY, M. J. 2004 Simulating the dynamics and interactions of flexible fibers in Stokes flows. J. Comput. Phys. 196 (1), 8–40.
- DE LA TORRE, J. G. & BLOOMFIELD, V. A. 1978 Hydrodynamic properties of macromolecular complexes. IV. Intrinsic viscosity theory, with applications to once-broken rods and multisubunit proteins. *Biopolymers* 17, 1605–1627.
- Wajnryb, E., Mizerski, K. A., Zuk, P. J. & Szymczak, P. 2013 Generalization of the Rotne-Prager-Yamakawa mobility and shear disturbance tensors. *J. Fluid Mech.* **731**, R3.
- Wandersman, E., Quennouz, N., Fermigier, M., Lindner, A. & Du Roure, O. 2010 Buckled in translation. Soft Matter 6 (22), 5715–5719.
- Wang, J., Tozzi, E. J., Graham, M. D. & Klingenberg, D. J. 2012 Flipping, scooping, and spinning: Drift of rigid curved nonchiral fibers in simple shear flow. *Phys. Fluids* **24** (12), 123304.
- WARNER, H. R. 1972 Kinetic theory and rheology of dilute suspensions of finitely extendible dumbbells. *Ind. Engng. Chem. Fundam.* 11 (3), 379–387.
- WITTEN, T. A. & DIAMANT, H. 2020 A review of shaped colloidal particles in fluids: Anisotropy and chirality.  $arXiv\ preprint\ arXiv:2003.03698$ .
- Yamakawa, H. 1970 Transport properties of polymer chains in dilute solution: Hydrodynamic interaction. J. Chem. Phys. 53, 436–443.
- YAMAMOTO, SATORU & MATSUOKA, TAKAAKI 1993 A method for dynamic simulation of rigid and flexible fibers in a flow field. J. Chem. Phys. 98 (1), 644–650.
- Yarin, A. L., Gottlieb, O. & Roisman, I. V. 1997 Chaotic rotation of triaxial ellipsoids in simple shear flow. *J. Fluid Mech.* **340**, 83–100.
- Young, Y.-N. & Shelley, M. J. 2007 Stretch-coil transition and transport of fibers in cellular flows. *Phys. Rev. Lett.* **99** (5), 058303.
- Zhang, X. & Graham, M. D. 2020 Multiplicity of stable orbits for deformable prolate capsules in shear flow. *Phys. Rev. Fluids* 5 (2), 023603.
- ZHANG, X., LAM, W. A. & GRAHAM, M. D. 2019 Dynamics of deformable straight and curved prolate capsules in simple shear flow. *Phys. Rev. Fluids* 4 (4), 043103.
- Zuk, P. J., Cichocki, B. & Szymczak, P. 2017 Intrinsic viscosity of macromolecules within the generalized Rotne-Prager-Yamakawa approximation. *J. Fluid Mech.* 822, R2.
- ZUK, P. J., CICHOCKI, B. & SZYMCZAK, P. 2018 GRPY: an accurate bead method for calculation of hydrodynamic properties of rigid biomacromolecules. *Biophys. J.* 115 (5), 782–800.
- Zuk, P. J., Wajnryb, E., Mizerski, K. A. & Szymczak, P. 2014 Rotne-Prager-Yamakawa approximation for different-sized particles in application to macromolecular bead models. *J. Fluid Mech.* **741**, R5.